# Petrogenesis of the Paleoproterozoic Näränkävaara layered intrusion, northern Finland, Part I : The northern peridotites and their relationships with the layered series and recharge events

Järvinen, Ville

2022-06-10

Järvinen , V , Halkoaho , T , Konnunaho , J , Heinonen , J S , Karinen , T & Rämö , O T 2022 , ' Petrogenesis of the Paleoproterozoic Näränkävaara layered intrusion, northern Finland, Part I : The northern peridotites and their relationships with the layered series and recharge events ' , Bulletin of the Geological Society of Finland , vol. 94 , no. 1 , pp. 23-52 . https://doi.org/10.17741/

http://hdl.handle.net/10138/344771
https://doi.org/10.17741/bgsf/94.1.002

Bulletin of the Geological Society of Finland, Vol. 94, 2022, pp 23–52 https://doi.org/10.17741/bgsf/94.1.002

# Petrogenesis of the Paleoproterozoic Näränkävaara layered intrusion, northern Finland, Part I: The northern peridotites and their relationships with the layered series and recharge events

Ville Järvinen[1]*, Tapio Halkoaho[2], Jukka Konnunaho[3], Jussi S. Heinonen[1], Tuomo Karinen[3] and O. Tapani Rämö[1]

[1]*Department of Geosciences and Geography, P.O. Box 64, FIN-00014 University of Helsinki, Finland*

[2]*Geological Survey of Finland, P.O. Box 1237, FIN-70211 Kuopio, Finland*

[3]*Geological Survey of Finland, P.O. Box 77, FIN-96101 Rovaniemi, Finland*

VERTAISARVIOITU
KOLLEGIALT GRANSKAD
PEER-REVIEWED
www.tsv.fi/tunnus

## Abstract

The Paleoproterozoic Näränkävaara layered intrusion, northern Finland, has a surface area of 25 km x 5 km and a stratigraphic thickness of ~3 km. The main body of the intrusion includes a 1.5–2 km thick basal dunite series and a 1.3 km thick peridotitic-dioritic layered series, the latter with two peridotitic reversals related to magma recharge. In addition, a series of poorly known elongate poikilitic harzburgitic intrusions (the northern peridotites) are found along the NE contact between the intrusion and the granite-gneiss basement complex. We investigate new mineral and whole-rock geochemical data from the northern peridotites, with the aim of clarifying their petrogenetic relationship to the main layered body of the intrusion. The northern peridotites form a 200–400 m thick cumulate series grading from olivine orthocumulates (OC) at the northern basement complex contact to olivine-orthopyroxene heteradcumulates (HAC) towards the main intrusion body in the south. The OC show whole-rock and mineral chemical trends consistent with origin as rapidly cooled olivine-melt mixtures. The HAC have crystallized in situ from a relatively Cr- and $SiO_2$-rich magma. Based on lithological and stratigraphical correlations, the northern peridotites are linked to the emplacement of the magma that caused the first reversal in the layered series: marginal orthocumulates were formed at the initial emplacement of a new pulse of LREE-enriched siliceous high-MgO basaltic (SHMB) magma into the Näränkävaara chamber, followed by heteradcumulate formation from a fractionating magma with added external $SiO_2$ and fluid. Ubiquitous granite-gneiss xenoliths and felsic veins in drill core suggest assimilation may have been a local process. The northern peridotite parental magma shows undepleted metal ratios suggesting no sulfide saturation occurred prior to emplacement.

Keywords: Näränkävaara, layered intrusion, heteradcumulate, reversal, marginal reversal, contamination

*Corresponding author (e-mail: ville.jarvinen@helsinki.fi)

Editorial handling: Jarmo Kohonen (e-mail: jarmo.kohonen@gtk.fi)

# 1. Introduction

Several mafic layered intrusions were emplaced in the NE Fennoscandian Shield during wide-spread 2.5–2.4 Ga mantle-plume related magmatism (Bayanova et al. 2019), with many of the intrusions hosting significant Ni-Cu-Co-PGE and Cr-V-Ti-Fe deposits (Alapieti & Lahtinen 1986; Alapieti et al. 1989; Huhtelin 2015; Iljina et al. 2015; Karinen et al. 2015). The 2.44 Ga mafic-ultramafic Näränkävaara intrusion, eastern Finland (Fig. 1), has a total stratigraphic thickness of ~3 km (Alapieti 1982; Järvinen et al. 2020, 2021). The main body of the intrusion is divided into two distinct magmatic series (Fig. 2b): (1) the basal dunite series, mainly composed of homogeneous olivine adcumulates, and (2) the layered series, composed of layered mafic-ultramafic cumulates (Järvinen et al. 2020, 2021). In addition to the main body, a series of elongate harzburgitic intrusions are found along the NE border of the intrusion. These are the subject of this study and referred to here as the northern peridotites – they are labeled in the inset in Fig. 2a, which also illustrates their distinctive ribbon-like expression in magnetometric maps.

The petrogenetic relationship between the northern peridotites and the main Näränkävaara intrusion body has remained elusive. The northern peridotites have been thought to represent satellite intrusions separate from the main Näränkävaara

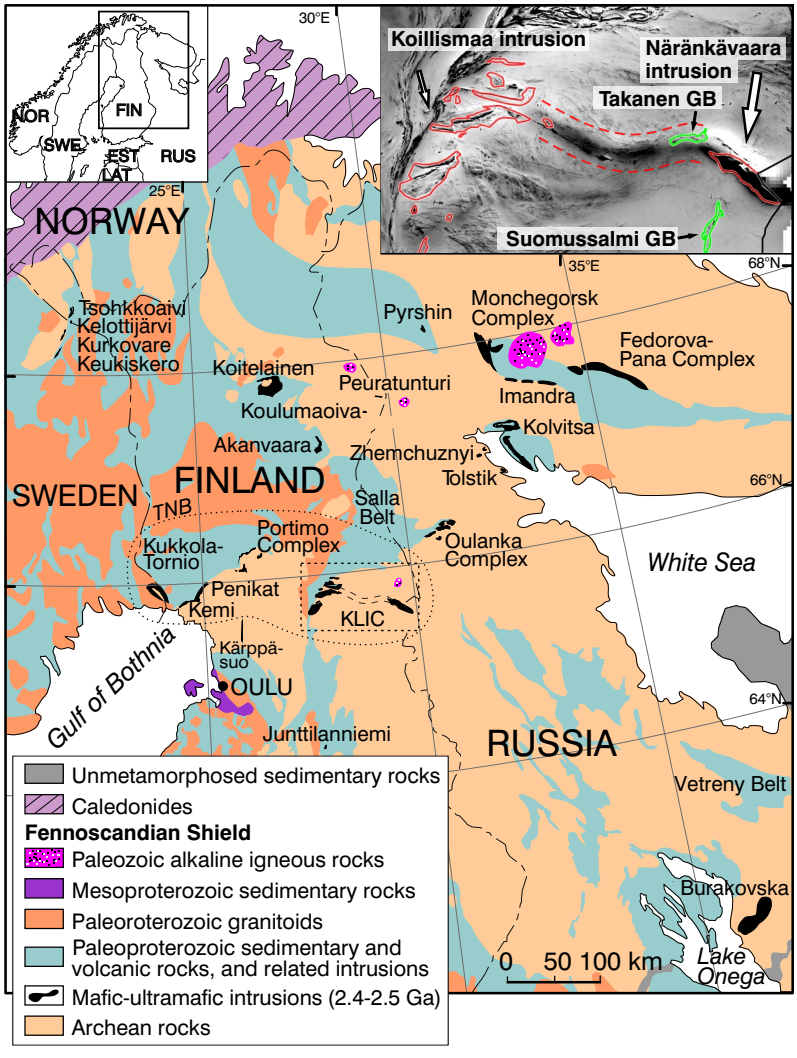


Figure 1. Map of 2.53–2.39 Ga mafic-ultramafic layered intrusions of the Fennoscandian Shield. Outlined are the Tornio-Näränkävaara belt of intrusions (TNB) (dotted line) and the Koillismaa-Näränkävaara Layered Intrusion Complex (KLIC) (dashed line). Inset shows KLIC on an aeromagnetic map (hill-shaded from the NE); Paleoproterozoic intrusions are outlined with red and the connecting "hidden dyke" geophysical anomaly with a red dash; Archean greenstone belts (GB) outlined in green. Map modified after Alapieti et al. (1990) and Karinen (2010).

intrusion, linked in turn either to the layered series (Alapieti et al. 1979) or to the basal dunite series (Alapieti 1982). Since the previous comprehensive studies from the area (Alapieti et al. 1979; Alapieti 1982), new data have been collected, which have largely been compiled and interpreted in two previous papers (Järvinen et al. 2020, 2021). Here, we aim to determine the petrogenetic relationship between the northern peridotites and the main Näränkävaara intrusion. A more in-depth review on the geology of the basal dunite and layered series of the Näränkävaara intrusion is presented in Part II of this study (Järvinen et al. 2022), along with an interpretation of the petrogenesis of the entire intrusion based on new U-Pb and Sm-Nd isotope data.

We present field and drill core observations to map the geology of the northern peridotites, use whole-rock and electron microprobe (EPMA) mineral chemical results to characterize their petrology, and investigate the processes of their emplacement and formation. Heteradcumulate cumulus textures have been presented as evidence for in situ crystallization processes in layered intrusions (Campbell 1978; Hepworth et al. 2017; Latypov et al. 2020). Our results suggest that the heteradcumulates in the northern peridotites formed primarily by in situ adcumulus growth in contact with a relatively Cr-rich magma, probably at the crystal-melt interface, similar to the "oikocrystites" in the Ntaka intrusion, Tanzania (Barnes et al. 2016). We connect the petrogenesis of the northern peridotites to the emplacement of the magma causing the first peridotitic reversal (PER-2) in the Näränkävaara layered series.

### *1.1. Terminology*

In this article, we use the cumulate terminology of Irvine (1982) and Latypov et al. (2020). Abbreviations for mineral names are from Whitney & Evans (2010). Cumulates are composed of liquidus crystals (i.e. cumulus/primocrysts) concentrated in bulk rock in high proportions relative to their parental liquid. The division between different types of cumulates is based on the proportions of texturally defined cumulus crystals: adcumulates contain >93 vol.% ; mesocumulates contain 93–75 vol.%; and orthocumulates contain 75–50 vol.% cumulus crystals (Irvine 1982). Heteradcumulates are characterized by poikilitic textures with finer-grained cumulus crystals (chadacrysts) enclosed in much coarser anhedral grains (oikocrysts), and thus texturally they are essentially ortho- or mesocumulates. In contrast to these, heteradcumulates are typically composed of high-temperature mineral assemblages with low quantities of low-temperature intercumulus phases, and show adcumulate-like whole-rock geochemistries poor in incompatible elements (Wager et al. 1960; Campbell 1987; Barnes et al. 2016; Latypov et al. 2020).

## 2. Geological background

### *2.1 Näränkävaara – the easternmost mafic-ultramafic intrusion of the Tornio-Näränkävaara belt*

The Näränkävaara intrusion is the easternmost member of both the Tornio-Näränkävaara belt of intrusions (TNB) and the Koillismaa-Näränkävaara Layered Intrusion Complex (KLIC) (Fig. 1) (Alapieti 1982). The TNB intrusions were emplaced in a continental rift setting at ~2.44 Ga, and they are currently positioned between the Archean basement complex and roughly contemporaneous supracrustal belts (Iljina & Hanski 2005), except for Näränkävaara, which is surrounded by Archean rocks. Several of the TNB intrusions show evidence of repeated magmatic recharge by basaltic magmas (Alapieti et al. 1990). The KLIC comprises the more mafic (pyroxenitic–gabbroic) Koillismaa intrusion blocks in the west, the more ultramafic (dominantly dunitic-pyroxenitic) Näränkävaara intrusion in the east, and a connecting unexposed gravity and magnetic anomaly called the "hidden dyke" (inset in Fig. 1) (Karinen et al. 2021). The KLIC has previously been dated at 2436 ± 5 Ma (Alapieti 1982).

The basal dunite series of the Näränkävaara intrusion shows the most primitive parental magma compositions determined from the KLIC (Järvinen et al. 2021), and its emplacement at 2442 ± 1 Ma likely marks the initiation of the KLIC magmatism (Järvinen et al. 2022). The KLIC probably represents a singular (now dismembered) ~100 km long magmatic system (Alapieti 1982; Järvinen et al. 2022).

Geophysics indicate that the Näränkävaara intrusion has a surface footprint of 25 x 5 km$^2$ (Fig. 2) and extends to a depth of 5–10 km (Elo 1992). The intrusion has steep contacts to the surrounding Archean granite-gneiss basement complex, except for a 50 m-thick volcanosedimentary sequence that is intersected near the NW tip of the intrusion (Vesanto 2003). A large fault splits the intrusion into the NW and SE blocks (Fig. 2a, note inset). Except for faulting, the intrusion is undeformed, and pristine or relict cumulus textures can typically be seen. The magmatic stratigraphy of the main body of the intrusion is determined from two drilling profiles (*A* and *D* in Fig. 2c) and is divided into two cumulate series (Järvinen et al. 2020, 2021):

1) The 1.5–2 km thick basal dunite series, composed of homogeneous dunite with minor peridotite and pyroxenite, with crystallization order Ol–Chr–Opx;
2) The 1.3 km thick layered series, which includes a peridotitic-pyroxenitic Ultramafic Zone (UMZ) at its lower part, and a gabbronoritic-dioritic Mafic Zone (MZ) in its upper part, with crystallization order Ol–Chr–Opx–Cpx–Pl.

In addition, two other poorly known ultramafic cumulate series are found at the borders of the intrusion:

1) the northern peridotites, clearly visible as narrow bands in the aeromagnetic map in Fig. 2a (see top-right inset);
2) a geochemically distinct dunite unit along the NE contact of the intrusion (cross-section *C* in Fig. 2c) (Akkerman 2008) – this unit is otherwise unknown and outside of the scope of this paper.

The basal dunite series can be divided into 3 zones based on lithology, labeled BD-1 to BD-3 in Fig. 2b (Järvinen et al. 2020). Zone BD-1 contains a ~200 m-thick olivine orthocumulate unit, in contact with (and including meter-sized xenoliths from) the southern basement complex. The olivine orthocumulates of zone BD-1 are incompatible element rich (10–50 ppm Zr), and are inferred as rapidly cooled mixtures of cumulus olivine and trapped high-MgO basaltic intercumulus melt (Järvinen et al. 2021). Recently, baddeleyites were separated from an olivine orthocumulate sample, and a concordant U-Pb age of 2441.7 ± 0.9 Ma was obtained indicating the initial emplacement age of the basal dunite series (Järvinen et al. 2022). Zones BD-2 and BD-3 are up to 1.8 km thick combined. They are composed mainly of homogeneous olivine adcumulates and olivine-orthopyroxene heteradcumulates typically with <3 vol.% intercumulus; minor mesocumulates and (olivine) orthopyroxenites are also found.

Geochemically, both BD-2 and BD-3 are very poor in incompatible elements. Olivine in the basal dunite ranges between Fo85-91.

The UMZ of the layered series contains harzburgites, followed by orthopyroxenites, websterites, and plagioclase-bearing websterites. The base of the MZ is defined by the appearance of cumulus plagioclase in a unit of melagabbronorite, followed by gabbronorites, gabbros and diorites. Three peridotitic units are found. The unit PER-1 at the base of the UMZ is a relatively thin unit of granular harzburgitic adcumulate. Units PER-2 and PER-3 are distinct olivine-rich units within more evolved cumulate sequences (Fig. 2b), and have been interpreted as reversals caused by new magma pulses (Alapieti 1982; Järvinen et al. 2020). PER-2 at the top of the UMZ is an olivine-orthopyroxene mesocumulate with poikilitic clinopyroxene and minor plagioclase and phlogopite; it is ~150 m thick and possibly emplaced in two separate pulses, as there is a pyroxenitic interlayer sandwiched between the two olivine-rich layers (Fig. 2b) (Alapieti 1982; Järvinen et al. 2020). PER-3 at the top of the MZ is a strongly altered lherzolite with disequilibrium

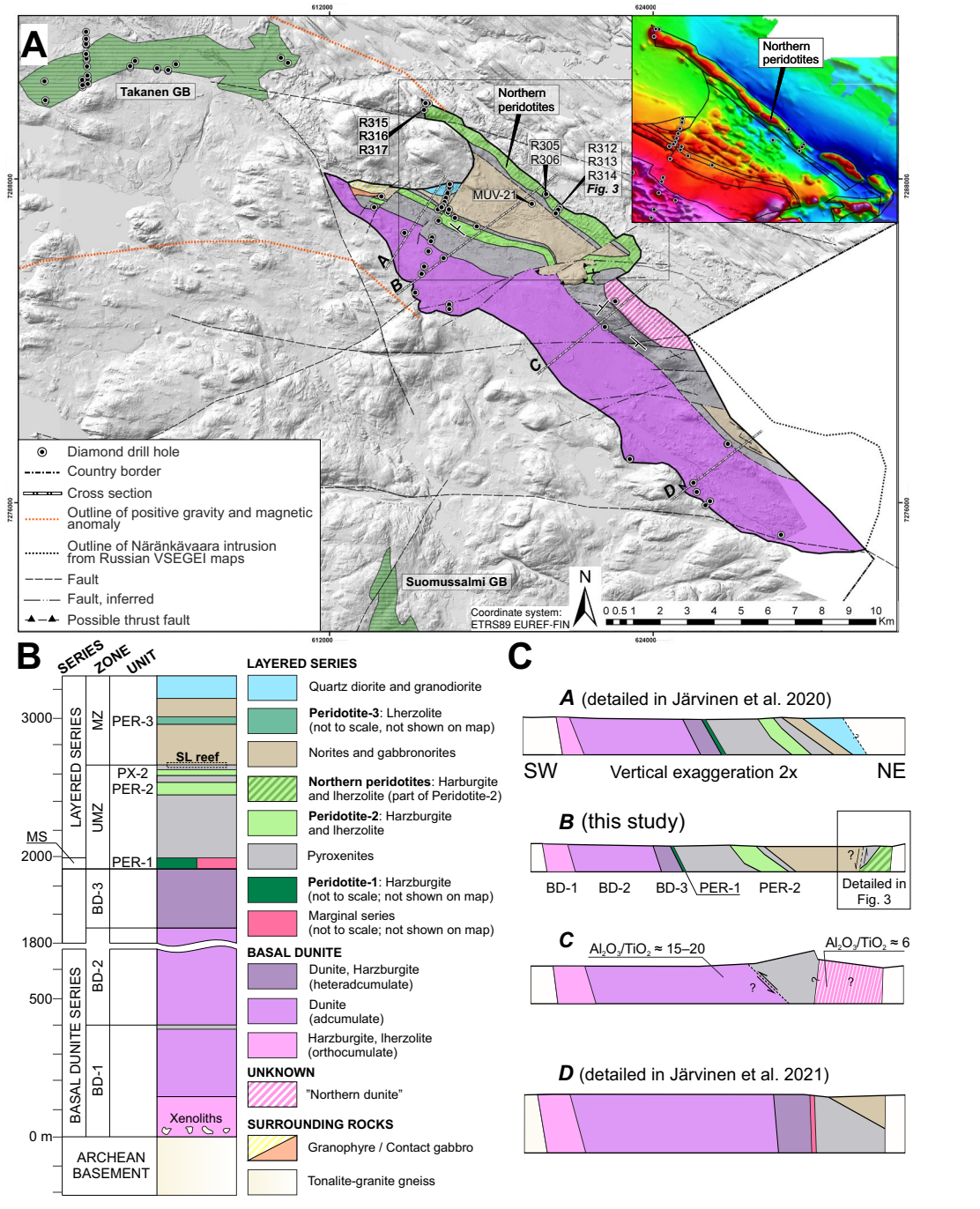


Figure 2. **a)** Simplified geological map of the Näränkävaara intrusion overlain on a hill-shaded digital elevation model. Archean basement complex surrounds the intrusion. The northern peridotites (labeled) are located along the NW contact of the intrusion, with intersecting drill holes labeled (see cross-section in Fig. 3). Aeromagnetic map in inset (red = high total magnetic intensity) illustrates the highly magnetic and elongate northern peridotites and the layered structure of NW part of the intrusion; dotted orange line outlines the "hidden dyke" geophysical anomaly. Intrusion outline in Russia compiled from online databases of the Russian Geological Research Institute (VSEGEI). **b)** Magmatic stratigraphic column of the Näränkävaara intrusion along cross-section *A*, with abbreviated unit names shown for relevant units, and the uneconomic PGE reef (labeled SL reef) outlined with dashed line. **c)** Representative cross-sections *A*–*D* across the Näränkävaara intrusion.

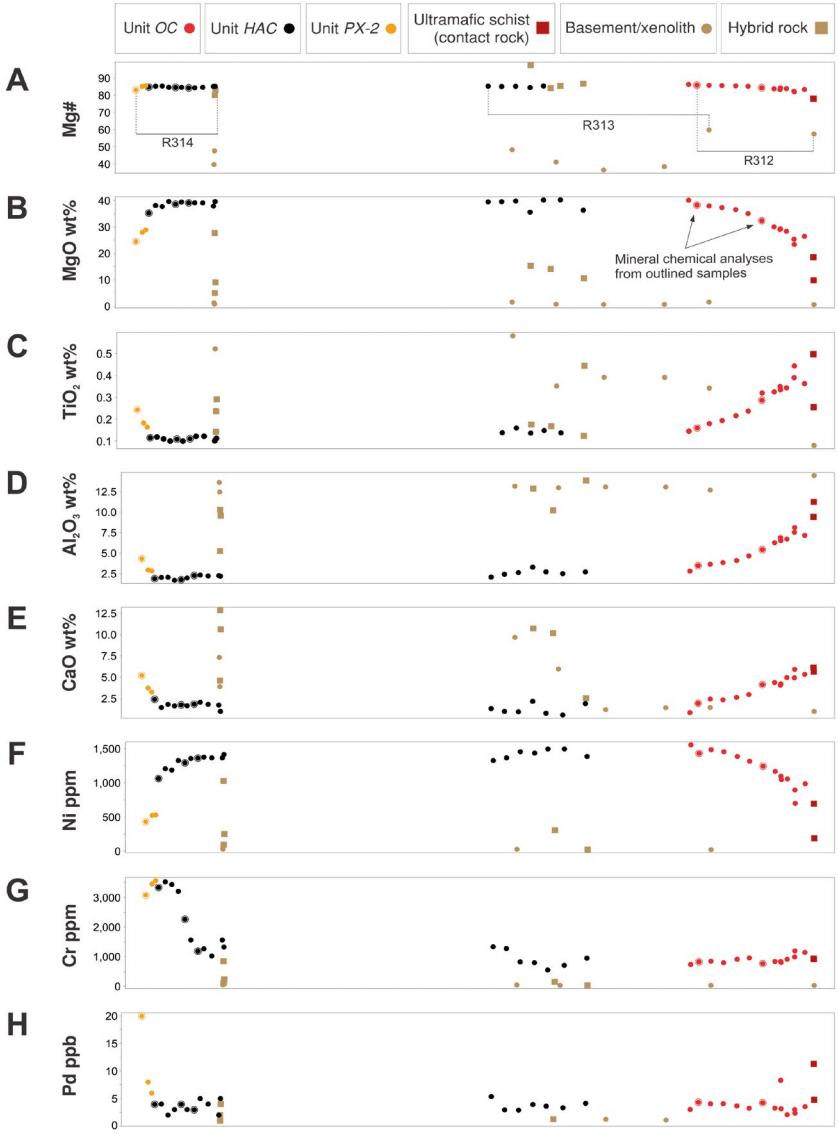


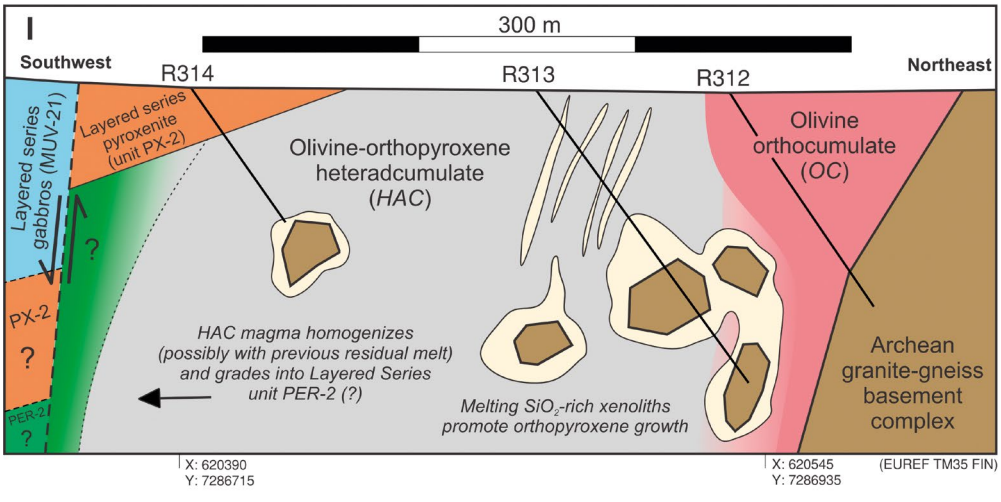


Figure 3. Cross-section across the NE contact of the Näränkävaara intrusion illustrating the geology of the northern peridotites (cross-section location indicated in Fig. 2). **a–h)** Whole-rock geochemical variations along cross-section. Note division into two units: 1) olivine orthocumulates in contact with the basement complex to the north (unit OC in text; red symbols), and 2) olivine-orthopyroxene heteradcumulates towards the layered series to the south (unit HAC in text; black symbols). Outlined symbols indicate locations of mineral chemical analyses. **i)** Generalized geology as interpreted from drill core logs, thin-section petrography, and whole-rock geochemistry (R312– 314 and MUV-21 are drill hole id's).

textures (e.g, exsolution, embayment, intergrowths, and secondary rims); it has probably formed by reaction between a relatively small volume of basaltic magma and the gabbros or residual liquid present in the MZ at the time of its emplacement. Average olivine Fo content of peridotitic units decreases upwards in stratigraphy (Fig. 2b): PER-1 with $Fo_{87.5}$, PER-2 with $Fo_{84}$, and PER-3 with $Fo_{82}$.

The layered series contains an uneconomic offset-type PGE reef (<0.5 ppm of Pd+Pt+Au) at the border of the UMZ and MZ, hosted by the first pyroxenitic unit (PX-2) immediately above the PER-2 reversal (labeled "SL reef" in Fig. 2b after the nearby Salmilammit-lake) (Järvinen et al. 2020).

## 2.2. The northern peridotites

The northern peridotites (labeled in Fig. 2a) were originally described by Alapieti et al. (1979), who mapped them as small ribbon-like poikilitic harzburgitic intrusions parallel to the northern contact of the intrusion, but separate from the main body (i.e. satellites). The northern peridotites were first correlated with the layered series unit PER-2 based on their similar textures, as both contain plagioclase (in contrast to unit PER-1 which is devoid of plagioclase; and PER-3 which was unknown). Unit PER-2 outcrops near the northern peridotites along the large NE-SW fault which splits the intrusion (Fig. 2a), and thus the emplacement of the PER-2 unit was hypothesized as a magmatic event coincident with the faulting (Alapieti et al. 1979). Later, however, the northern peridotites were correlated to the basal dunite series (Alapieti 1982), probably because of their notable lithologic similarity to the southernmost olivine orthocumulate margin of the basal dunite series, described previously (BD-1 in Fig. 2b). The basal dunite was envisaged to envelop the layered series in a funnel shape along its northern and southern borders (Alapieti 1982), somewhat analogous to the structure of the Great Dyke (Wilson 1996). Since then, the northern peridotites were drilled for mineral exploration purposes (Iljina 2003), but the results were not otherwise investigated in detail until this paper. As originally suggested by Alapieti et al. (1979), we also interpret the northern peridotites to have formed from emplacement of the PER-2 magma, as discussed later.

# 3. Materials & Methods

The materials at hand mostly come from nine mineral exploration drill holes located along the NW margin of the Näränkävaara intrusion (labeled in Fig. 2a) (Iljina 2003). Compiled materials include drill core and core logs, thin sections, and results of whole-rock and mineral chemical analyses (Vesanto 2003; Lahtinen 2005; Telenvuo 2017). Five new outcrop samples were collected by the study team in 2017–2018.

All samples are enumerated and all analysis results are listed in the attached electronic supplementary materials (S1), along with method descriptions, standards used, and data on detection limits and precision.

## 3.1. Whole-rock geochemistry

Including new and previous sampling, a total of 89 whole-rock analyses have been made at the Labtium Oy laboratories in Finland. Methods are described in brief; for complete method descriptions see quoted method codes in Rasilainen et al. (2007). Whole-rock compositions described in this study are normalized to volatile-free 100 wt.%. Ratio of whole-rock FeO to $Fe_2O_3$ was found to be insignificant for presented interpretations and all iron has been treated as FeO (see alternative FeO recalculation methods for olivine-rich cumulates in e.g. Barnes et al. 2007). The magnesium-number (Mg#) is calculated as $100*[MgO/40.3044/(MgO/40.3044+FeO_{total}/71.844)]$.

All samples were analyzed with X-ray fluorescence (XRF; method code 175X) from pressed rock-powder pellets using a wavelength dispersive spectrometer (elements Si, Ti, Al, Fe, Mn, Mg, Ca, Na, K, P, Cl, Cr, Cu, Ni, Rb, S, Sc, Sn, Sr, Th, U, V, Y, Zn, Zr). Precious metals (Au, Pd, Pt) were

analyzed for almost all samples using either the Pb-fire assay preparation method followed by graphite furnace atomic absorption spectrometry with electrochemical atomization (GFAAS; method code 704U), or an aqua regia partial leach preparation followed by GFAAS (method code 521U); detection limits are 1–2 ppb and 0.5–1 ppb respectively. The rare earth elements (REE) and other trace elements (La, Ce, Pr, Nd, Sm, Eu, Gd, Tb Dy, Ho, Er, Tm, Yb, Lu, Hf, Y, Nb, Ta, Rb, Th, U) were determined for 11 samples, prepared by $HClO_4$–HF and $HNO_3$–$H_2O_2$ dissolution and lithium metaborate-sodium perborate fusion and final dissolution with $HNO_3$, followed by analysis with either inductive coupled mass spectrometry (ICP-MS; method code 308M), or for some elements (Co, Sc, V, and Zr) with inductively coupled plasma atomic emission spectrometry (ICP-AES; method code 308P); detection limits are generally 1–2 ppm for the REE and 2–5 ppm for other elements.

## 3.2. Mineral chemistry

Mineral chemical analyses were made from 12 polished thin-sections (in total, 577 spots) at the GTK mineralogical laboratories with a Cameca SX100 electron microprobe. Accelerating voltage for pyroxenes and plagioclase was 15 kV, beam current 20 nA, and beam diameter 5 µm; for olivine 20 kv, 60 nA, and 5 µm; and for chromite 15 kV, 40 nA, and 5 µm, respectively. Counting times were 10–60 s depending on the analyzed element. Natural standard measurements indicate 3σ errors generally in range of 0.2–0.5 wt.% (e.g., olivine Mg# ± 0.4). Spot analyses across orthopyroxene grains (i.e. core-rim analyses) have been made from 12 grains in 7 samples (total of 104 spots). Ferric iron in spinel has been estimated by recalculation assuming stoichiometry with the method of Barnes (1998). For spinels, Mg# = Mg/(Mg+$Fe^{2+}$); Cr# = Cr/(Cr+Al); and $Fe^{3+}$# = $Fe^{3+}$/(Cr+Al+$Fe^{3+}$).

# 4. Results

## 4.1. Petrography and geochemistry of the northern peridotites

The NE contact zone of the Näränkävaara intrusion is intersected by 8 drill holes (labeled in Fig. 2a), with a schematic cross-section presented in Fig. 3i. This cross-section intersects the northern peridotites and their contacts both to the Archean granite-gneiss complex in the north and to the layered series pyroxenite in the south. Combined with geophysical surveys (Elo 1992), it indicates that the peridotites are 200–400 m thick. Gabbros intersected in drill hole MUV-21 (Fig. 2a) and magnetometric surveys (inset in Fig. 2a) (Vesanto 2003) clearly demonstrate uninterrupted continuity of the layered series up to the northern granite-gneiss contact, indicating that the northern peridotites are not satellite intrusions separate from the main Näränkävaara intrusion as Alapieti (1982) anticipated.

The northern peridotites are divided into two units based on petrography and geochemistry. The peridotites are variably serpentinized but typically show well-preserved cumulus textures (Fig. 4a, b). The unit located nearest to the contact with the basement complex is composed of olivine orthocumulates (unit named *OC* in Fig. 3), with intercumulus pyroxenes, plagioclase and phlogopite (Fig. 4a). At the immediate contact is a 1–2 m thick strongly altered and tectonized ultramafic schist (labeled "contact rock" in Fig. 3 and other figures). Away from the contact, the amount of olivine increases and clinopyroxene decreases, as the cumulates grade from olivine-pyroxenites into lherzolites and finally into harzburgites towards the south. Increase in modal olivine (typically 40–75 vol.% with a maximum of 85 vol.%) is reflected in the increase of whole-rock MgO and Ni (Figs. 3b, f), with decrease in clinopyroxene similarly reflected in decrease of $Al_2O_3$ and CaO (Figs. 3d, e). Pyroxenes become coarser grained and poikilitic (2–20 mm) with distance from the contact against the basement complex. Cumulus olivines are eu- to subhedral

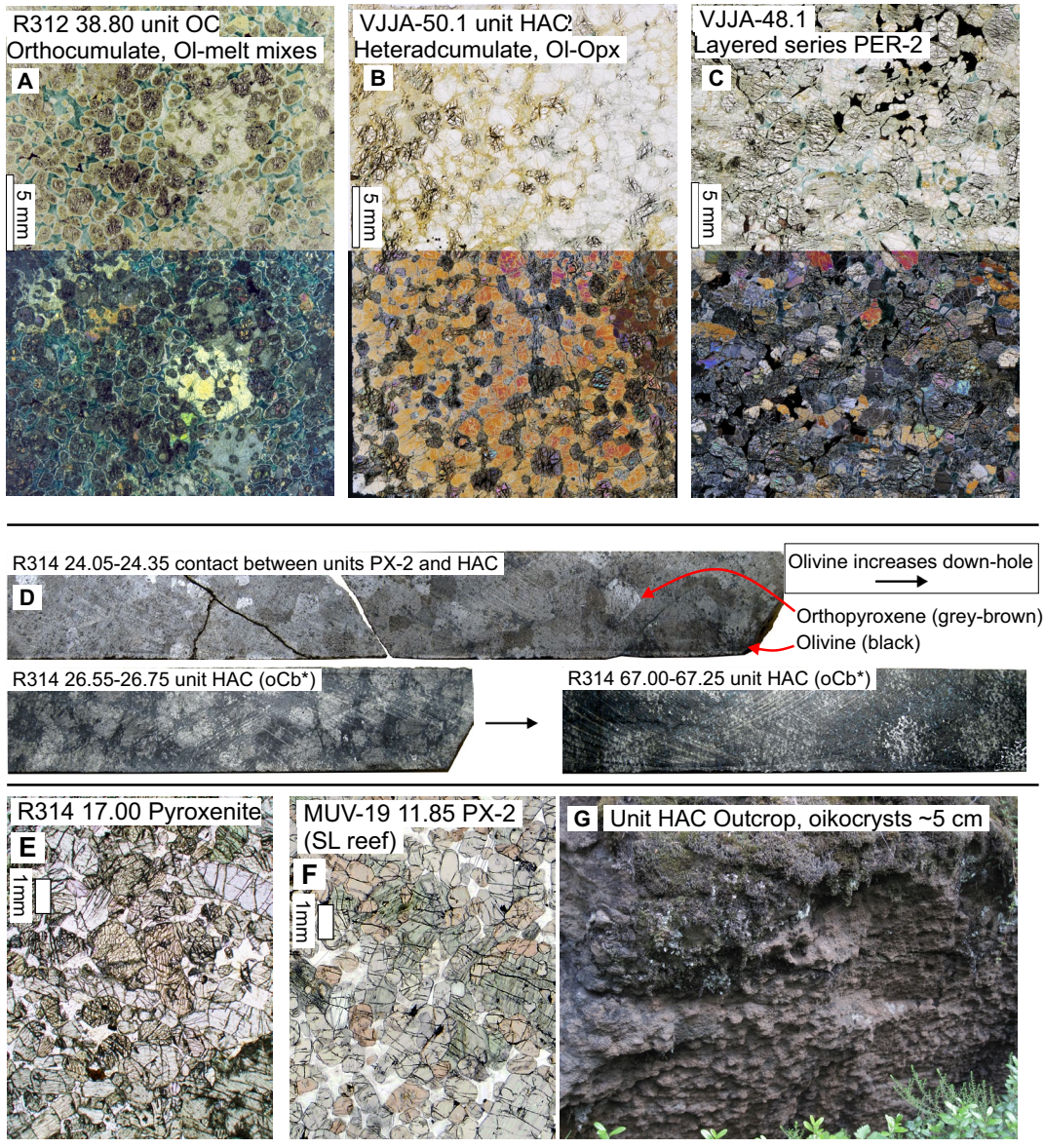


Figure 4. Photographs of ultramafic cumulates from the Näränkävaara intrusion **a–c)** Thin-section photographs; upper halves are plane-polarized, lower halves are cross-polarized, scale bar is 5 mm **a)** Moderately serpentinized olivine orthocumulate of northern peridotite unit OC (Fig. 3); intercumulus consists of (poikilitic) pyroxenes and minor plagioclase and phlogopite (the latter two mostly altered). **b)** Almost unaltered olivine-orthopyroxene heteradcumulate of northern peridotite unit HAC (Fig. 3); sample is an extreme "oikocrystite" composed almost purely of olivine and up to 5 cm orthopyroxene oikocrysts (also in g); olivine chadacrysts are embayed. **c)** Olivine-orthopyroxene mesocumulate of unit PER-2 of the layered series (Fig. 2b); intercumulus consist of clinopyroxene, plagioclase and black (oxide-altered) phlogopite. **d)** Drill core photos from R314 in Fig. 3 detailing the contact between the northern peridotite unit HAC (in b) and the pyroxenitic unit PX-2 of the layered series (in e, f). Towards the layered series in the south, olivine mode decreases with grains becoming finer and increasingly embayed; orthopyroxene mode increases while also decreasing in grain size. Between 25–22 m the rocks grade from poikilitic olivine-pyroxenites into granular orthopyroxene cumulates; at 17 m the rocks are completely unaltered plagioclase-websterites (in **e**; plane polarized thin-section photograph), almost identical to those found in the unit PX-2 of the layered series (in **f**). **g)** Outcropping poikilitic harzburgite of unit HAC; the distinct texture is caused by abundant coarse orthopyroxene oikocrysts about 5–10 cm in size.

(1–3 mm), but chadacrysts in orthopyroxene are finer grained (0.5–1 mm) with typically embayed grain boundaries.

The OC unit grades into the second unit named *HAC* for heteradcumulate (Fig. 3), which is composed of relatively homogeneous olivine-orthopyroxene heteradcumulates. The HAC unit is characterized by very coarse (10–50 mm) poikilitic orthopyroxene (Fig. 4b). Olivine chadacrysts (0.5–2 mm) typically show embayed grain boundaries (Fig. 4b). On thin section scale textures are typically bimodal, with either 20–40 vol.% coarse poikilitic orthopyroxene enclosing olivine, or, outside of the oikocrysts, characterized by similar olivine-rich textures as the OC unit (with intercumulus plagioclase, phlogopite, and minor clinopyroxene). However, at the extreme, "oikocrystites" are found, composed almost entirely of up to 5 cm orthopyroxene oikocrysts and chadacryst olivine (Fig. 4b) – in outcrop, homogeneous "oikocrystites" are found to be continuous for at least tens of meters (Fig. 4g). Zoning has not been found in pyroxenes using optical petrography. In the southern part of the cross-section in Fig. 3, a gradational magmatic contact between the HAC unit and an unaltered plagioclase-websterite is intersected in drill hole R314 (Figs. 4d, e). The gradual contact from the relatively olivine-rich HAC unit into the pyroxenites is reflected in decreasing whole-rock Ni and increasing Cr (Fig. 3g, f).

Small equant chromite inclusions (~50 µm) are commonly found in olivine in both the OC and HAC units. Otherwise, chromite is very rare in the OC unit. Fine-grained euhedral chromite is relatively commonly found as inclusions in orthopyroxenes in the HAC unit, with rare euhedral grains up to 0.5 mm found in intercumulus; chromite mode varies between adjacent drill-hole samples but never exceeds trace amounts. Trace amounts of pentlandite and pyrrhotite (<0.1 mm) are found, commonly intergrown with late magmatic or secondary (Fe-Ti-V-Zn) oxides.

Several granite-gneiss xenoliths (up to 1 m in drill core) showing partial melting textures, and irregular felsic veins interpreted as partial melts, are intersected in the HAC unit (Fig. 3). Strongly altered peridotite samples can be found near the xenolith and vein contacts in the HAC unit, as well as near the granite-gneiss contact in the OC unit; peridotite samples (hybrid rocks) from these locations show untypically high concentrations of $K_2O$, $Na_2O$, Ba, Rb, Sr, and Pb (Fig. 3; see S2 for other elements).

## 4.2. Whole-rock geochemical variation

Whole-rock geochemistry of representative samples from the northern peridotites are compiled in Table 1, with comparisons to relevant units from the layered series. Geochemical variations in the OC and HAC units are illustrated in Figs. 5 and 6. Both the OC and HAC units have high MgO (23–40 wt.%) and Ni (700–1490 ppm) reflecting their olivine-rich compositions. Both units show similar Mg# (~83–85) and Ni (~1000–1500 ppm) values for the most MgO-rich samples (>30 wt.% MgO). Both units have average $Al_2O_3/TiO_2$ of 20 (Table 1), similar to the layered series and basal dunite series (Järvinen et al. 2020, 2021).

Chemistry of the OC unit primarily reflects variations in modal olivine, with a large range in MgO (23–38 wt.%). Olivine-incompatible elements plot along straight trend lines relative to MgO (red in Figs. 5 and 6), except for some large ion lithophile elements (LILE), which scatter likely due to mobility during serpentinization (see S2 for full set of geochemical plots). Figures 5 and 6 indicate that the OC unit is essentially composed of binary olivine-melt mixtures, with the trend lines indicating that the composition of the trapped melt component approximates that of the ultramafic schists at the immediate contact (a possible chilled margin), and also that of the Näränkävaara marginal series.

In comparison, the HAC unit shows adcumulate chemistry with much less geochemical variance against MgO, and low concentrations of incompatible elements (black in Figs. 5 and 6). The relatively high Cr-values reflect high modal

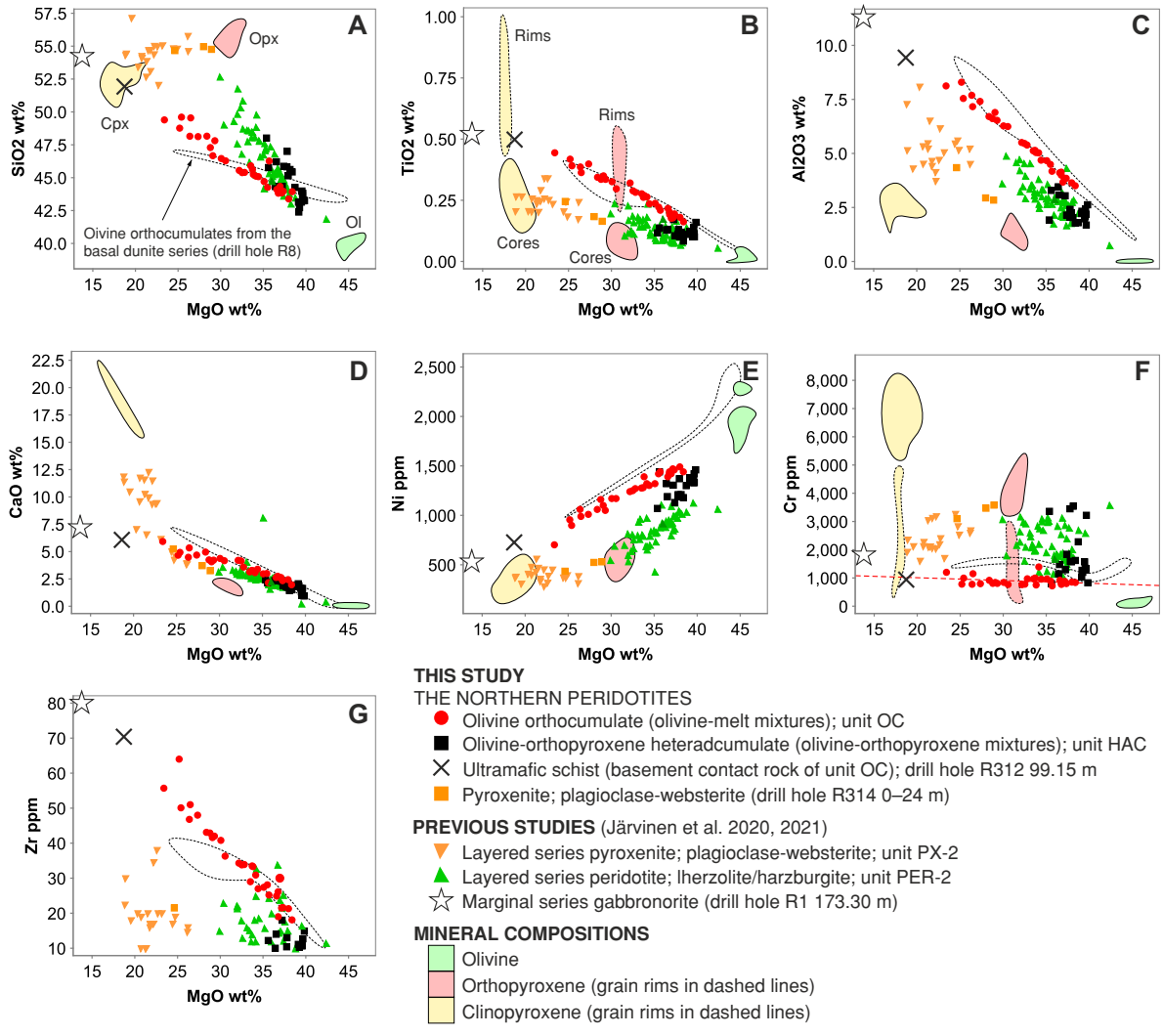


Figure 5. **a–g)** Whole-rock geochemical variations in the northern peridotites of the Näränkävaara intrusion, with comparisons to selected units of the layered series (Järvinen et al. 2020). Mineral compositions analyzed from the two studied cumulate units (see Fig. 3) shown in colored fields. Note that samples from the northern peridotite OC unit (red) plot as olivine-melt mixtures, while samples from the HAC unit (black) plot as olivine-orthopyroxene mixtures with a minor melt component (estimated at 0–15 vol.%). Dashed line shows compositions of olivine orthocumulates from the Näränkävaara basal dunite series, in contact with the basement complex to the south of the intrusion (Fig. 2); these samples have also been interpreted as olivine-melt mixtures (Järvinen et al. 2021).

orthopyroxene, with the highest Cr-values (<3540 ppm) found below the contact with the pyroxenites in drill hole R314 (Figs. 3g and 5f).

Molecular ratios in Fig. 7 suggest that whole-rock geochemistry of the OC unit is controlled by addition and subtraction of olivine with an average composition of $Fo_{87.4}$; whereas the HAC unit is controlled by combined olivine and orthopyroxene addition and subtraction with an average olivine composition of $Fo_{84.1}$ (note similarity to the layered series unit PER-2).

REE and trace-element patterns for the OC and HAC units (Fig. 8) show relatively high LREE, LILE, and Th-U concentrations with low Nb–Ta, similar to other 2.44 Ga intrusions contaminated with felsic continental crust (e.g., Kulikov et

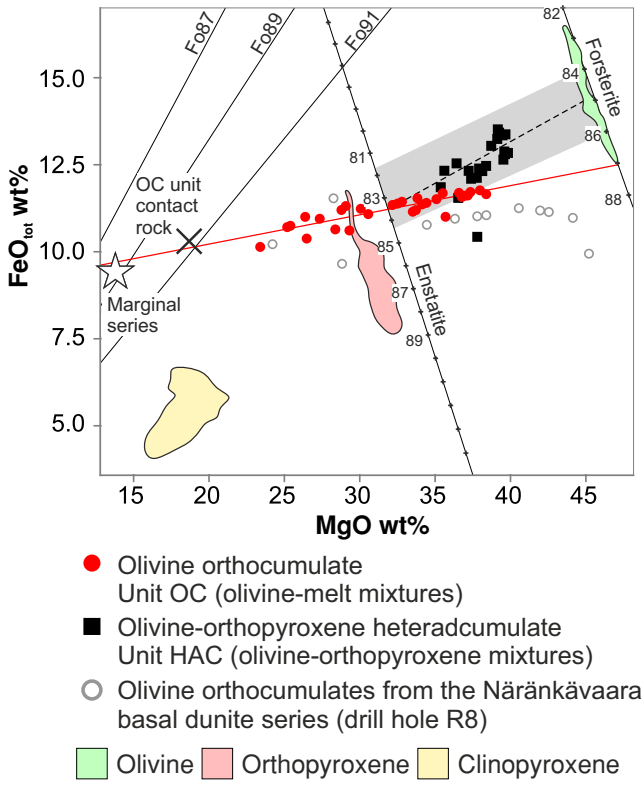


Figure 6. Whole-rock MgO vs. $FeO_{tot}$ variations in the northern peridotite series of the Näränkävaara intrusion. Analyzed mineral compositions shown in red, green and yellow-colored fields (see sample locations in Fig. 3). Labeled tick-marks indicate calculated pure Fo and En compositions; labeled unticked lines indicate compositions of liquids in equilibrium with olivine $Fo_{87\text{-}91}$ ($K_D$ Fe/Mg Ol/Melt 0.30; Roeder & Emslie 1970). Regression line through OC unit sample points (red) suggests that the unit is composed of mixtures of $Fo_{87}$ olivine and a trapped melt component with similar composition to the Näränkävaara marginal series (parental magma MgO of 13–15 wt.%). HAC unit (black) plots as olivine-orthopyroxene mixtures; dashed line connects average analyzed olivine ($Fo_{84.8}$) and orthopyroxene ($En_{83.3}$) compositions (grey field shows full range of analyzed compositions). Olivine orthocumulates from the Näränkävaara basal dunite series are shown in grey circles for comparison (Järvinen et al. 2021).

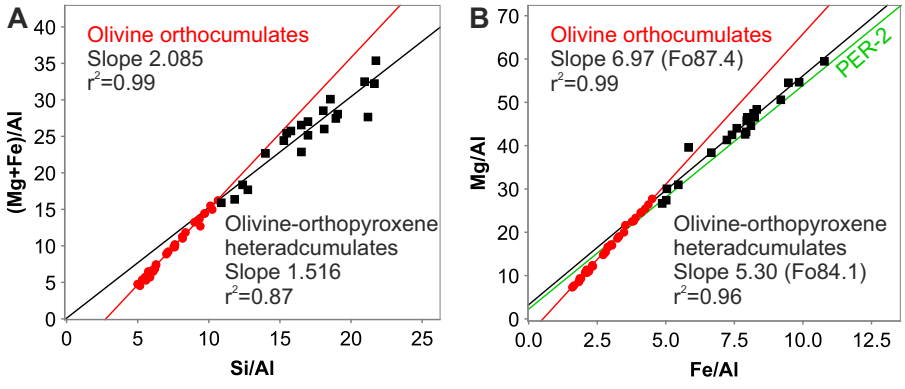


Figure 7. Molecular ratio plots of whole-rock samples from the northern peridotites of the Näränkävaara intrusion. **a)** Unit OC (red) shows Al-normalized (Mg+Fe)/Si ratio of 2.085 – essentially the same as 2.0 for pure olivine – suggesting the whole-rock compositions of these rocks are controlled by addition and subtraction of olivine (Pearce 1968; Chai & Naldrett 1992). Unit HAC (black) shows a ratio of 1.5, interpreted as olivine+orthopyroxene control (ratio for pure orthopyroxene would be 1.0 on this plot). **b)** Estimation of olivine Mg#'s from Al-normalized whole-rock Mg-Fe ratios (Makkonen et al. 2017). For unit OC estimate is $Fo_{87.4}$ and for HAC $Fo_{84.1}$, note similarity of the latter to layered series unit PER-2 shown in green.

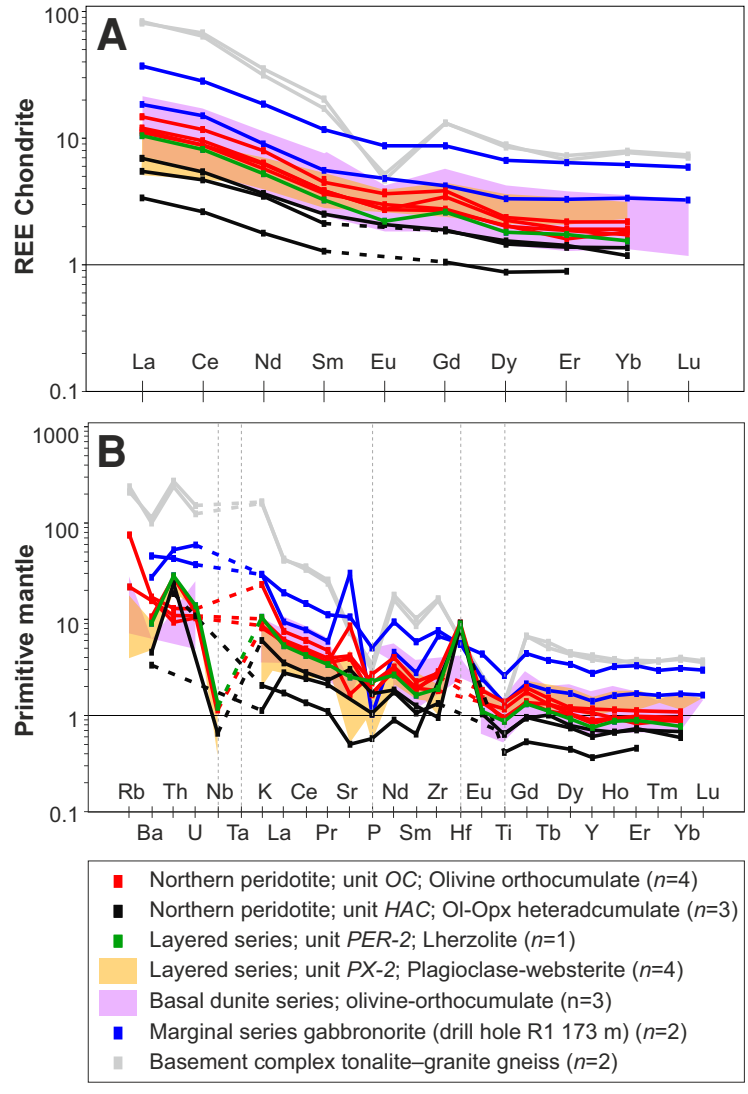


Figure 8. Whole-rock trace element compositions of the northern peridotites of the Näränkävaara intrusions on **a)** REE and **b)** trace element diagrams, with comparisons to other key units in the intrusion (Järvinen et al. 2020, 2021); normalization factors from Nakamura (1974) and McDonough & Sun (1995).

al. 2010). In both units, total REE abundances correlate negatively with MgO (see S2), indicating a small trapped melt component in the HAC unit as well (ranging between 0–15 wt.%). The peculiar positive Hf-anomaly (Fig. 8b) has been observed previously in the Finnish 2.44 Ga mafic intrusions and remains unresolved (Maier et al. 2018; Järvinen et al. 2020).

Both OC and HAC units are unmineralized. Sulfur generally ranges between 150–700 ppm, with an average of 400 ppm in OC and 300 ppm in HAC (both with <0.2 vol.% normative sulfide). Nickel (700–1490 ppm) is hosted mainly by olivine. Palladium ranges between 1–5 ppb, while platinum values are low or below detection limits (Fig. 3h). Highest S (1090 ppm), Cu (290 ppm), and Pd (11 ppb) are found in an ultramafic schist in immediate contact with the basement complex (labeled "contact rock" in Table 1, and Figs. 3 and 5).

The pyroxenites in R314 contain anomalous Pd and Pt (20 and 14 ppb, respectively), but otherwise plot as typical Näränkävaara layered series pyroxenites (Fig. 5); they are compared to the PGE-enriched pyroxenites of the layered series unit PX-2 in Table 1 (see "SL reef" in Fig. 2b).

**Table 1**: Results of representative whole-rock analyses from the Näränkävaara intrusion

| Series | Northern peridotites | | | | | | | Layered series | | Marginal series |
|---|---|---|---|---|---|---|---|---|---|---|
| Sample | *1* | *2* | *3* | *4* | *5* | *6* | *7* | *8* | *9* | *10* |
| Unit | OC | OC | OC | HAC | HAC | HAC | see R314 in Fig. 3 | PER-2 | PX-2 | |
| Rock type | Ultramafic schist (contact | Lherzolite | Lherzolite | Harzburgite | Harzburgite | Harzburgite | Plagioclase-Websterite | Lherzolite | Pl-Websterite | Gabbronorite |
| Cumulus name | non-cumulus | oMCb*a*(pfc) | oMCb*a*(pfc) | oMCb*(paf) | oMCb*(apf) | oOCb*(apf) | bMCa*p | obMCa*(pf) | bMCa*p | non-cumulus |
| $SiO_2$ wt% | 49,00 | 40,20 | 37,65 | 37,90 | 38,21 | 45,20 | 53,50 | 38,36 | 48,31 | 52,12 |
| $TiO_2$ | 0,47 | 0,21 | 0,15 | 0,14 | 0,11 | 0,11 | 0,24 | 0,15 | 0,23 | 0,50 |
| $Al_2O_3$ | 8,90 | 4,18 | 3,12 | 2,30 | 2,98 | 1,81 | 4,25 | 2,48 | 5,02 | 10,89 |
| $FeO_t$ | 9,72 | 10,17 | 9,86 | 11,25 | 10,81 | 11,16 | 9,63 | 11,32 | 7,51 | 9,04 |
| MnO | 0,16 | 0,16 | 0,14 | 0,15 | 0,16 | 0,20 | 0,20 | 0,18 | 0,17 | 0,16 |
| MgO | 17,50 | 30,70 | 31,39 | 34,90 | 31,40 | 33,30 | 24,10 | 30,83 | 19,47 | 13,24 |
| CaO | 5,79 | 3,02 | 2,24 | 0,82 | 2,01 | 2,29 | 5,12 | 1,95 | 10,64 | 6,91 |
| $Na_2O$ | 1,91 | 0,24 | 0,14 | <0.03 | 0,35 | <0.03 | 0,58 | 0,14 | 0,28 | 2,24 |
| $K_2O$ | 0,83 | 0,26 | 0,20 | 0,13 | 0,15 | 0,06 | 0,23 | 0,26 | 0,05 | 0,81 |
| $P_2O_5$ | 0,08 | 0,04 | 0,03 | 0,03 | 0,03 | 0,01 | 0,02 | 0,04 | 0,02 | 0,10 |
| Total | 94,36 | 89,18 | 84,92 | 87,62 | 86,21 | 94,14 | 97,87 | 85,71 | 91,70 | 96,01 |
| $Al_2O_3/TiO_2$ | 18,9 | 19,9 | 20,8 | 16,4 | 27,1 | 16,5 | 17,7 | 16,5 | 21,8 | 21,7 |
| Mg# | 76,2 | 84,3 | 85,0 | 84,7 | 83,8 | 84,2 | 81,7 | 82,9 | 82,2 | 72,3 |
| Ba ppm | 170 | 103 | 70 | 52 | 30 | 36 | 86 | 60 | <20 | 300 |
| Cl | 428 | 710 | 900 | 1660 | 800 | 486 | <100 | 600 | <100 | 2300 |
| Cr | 941 | 958 | 860 | 828 | 1150 | 3360 | 3100 | 1680 | 3050 | 1820 |
| Cu | 290 | 29 | 30 | 22 | <20 | <20 | 32 | <20 | 30 | 70 |
| Ni | 696 | 1302 | 1420 | 1460 | 1320 | 1070 | 435 | 920 | 430 | 530 |
| Rb | 29 | 13 | <10 | <10 | <10 | <10 | 11 | <10 | <10 | <10 |
| S | 1090 | 410 | 600 | 468 | 500 | <100 | <100 | 300 | 600 | 600 |
| Sr | 128 | 83 | 170 | 21 | 60 | 19 | 55 | 50 | 10 | 210 |
| V | 141 | 64 | 50 | 48 | 40 | 57 | 111 | 50 | 120 | 140 |
| Zn | 167 | 79 | 70 | 78 | 90 | 103 | 72 | 90 | 70 | 80 |
| Zr | 70,4 | 27,0 | 30,0 | 14,9 | 10,0 | <10 | 21,5 | 20,0 | 10,0 | 80,0 |
| La | n.a. | 3,95 | 3,78 | n.a. | 2,28 | n.a. | n.a. | 3,44 | 2,72 | 12,20 |
| Ce | n.a. | 8,24 | 7,60 | n.a. | 4,68 | n.a. | n.a. | 7,04 | 5,91 | 24,40 |
| Pr | n.a. | 1,00 | 0,92 | n.a. | 0,59 | n.a. | n.a. | 0,86 | 0,82 | 2,83 |
| Nd | n.a. | 4,00 | 3,62 | n.a. | 2,30 | n.a. | n.a. | 3,30 | 3,77 | 11,70 |
| Sm | n.a. | 0,78 | 0,74 | n.a. | 0,51 | n.a. | n.a. | 0,66 | 0,96 | 2,37 |

| | | | | | | | | | | |
|---|---|---|---|---|---|---|---|---|---|---|
| Eu | n.a. | 0,21 | 0,23 | n.a. | 0,16 | n.a. | n.a. | 0,17 | 0,29 | 0,67 |
| Gd | n.a. | 0,95 | 0,76 | n.a. | 0,52 | n.a. | n.a. | 0,72 | 1,12 | 2,40 |
| Tb | n.a. | 0,13 | 0,11 | n.a. | <0.1 | n.a. | n.a. | 0,11 | 0,18 | 0,37 |
| Dy | n.a. | 0,77 | 0,69 | n.a. | 0,50 | n.a. | n.a. | 0,62 | 1,15 | 2,29 |
| Ho | n.a. | 0,14 | 0,14 | n.a. | 0,10 | n.a. | n.a. | 0,13 | 0,24 | 0,48 |
| Er | n.a. | 0,43 | 0,42 | n.a. | 0,31 | n.a. | n.a. | 0,39 | 0,72 | 1,44 |
| Tm | n.a. | <0.1 | <0.1 | n.a. | <0.1 | n.a. | n.a. | <0.1 | <0.1 | 0,2 |
| Yb | n.a. | 0,42 | 0,38 | n.a. | 0,30 | n.a. | n.a. | 0,34 | 0,63 | 1,36 |
| Lu | n.a. | <0.1 | <0.1 | n.a. | <0.1 | n.a. | n.a. | <0.1 | <0.1 | 0,2 |
| Hf | n.a. | n.a. | 2,59 | n.a. | 2,42 | n.a. | n.a. | 2,53 | 2,58 | 1,55 |
| Zr | n.a. | n.a. | 21 | n.a. | 13 | n.a. | n.a. | 21 | 16 | 60 |
| Y | n.a. | 4,57 | 3,56 | n.a. | 2,60 | n.a. | n.a. | 3,23 | 5,99 | 11,80 |
| Nb | n.a. | n.a. | 0,75 | n.a. | 0,43 | n.a. | n.a. | 0,80 | 0,49 | <3 |
| Ta | n.a. | n.a. | <0.2 | n.a. | <0.2 | n.a. | n.a. | <0.2 | <0.2 | <1 |
| Rb | n.a. | n.a. | 8,34 | n.a. | 4,91 | n.a. | n.a. | 8,49 | 3,99 | 29,60 |
| Th | n.a. | 0,87 | 2,16 | n.a. | 1,87 | n.a. | n.a. | 2,25 | 1,71 | 3,40 |
| U | n.a. | 0,22 | 0,24 | n.a. | <0.2 | n.a. | n.a. | 0,28 | <0.2 | 0,75 |
| Sc | n.a. | 12,2 | 9,0 | n.a. | 9,5 | n.a. | n.a. | 11,3 | 38,3 | 23,8 |
| V | n.a. | n.a. | 51 | n.a. | 42 | n.a. | n.a. | 56 | 139 | 150 |
| Co | n.a. | n.a. | 122 | n.a. | 134 | n.a. | n.a. | 126 | 71 | 58 |
| Au ppb | 85,1 | n.a. | 1,1 | 1,4 | 1,3 | 10,0 | 2,0 | <2 | 8,0 | 2,4 |
| Pd | 11,3 | n.a. | 2,0 | 2,9 | 4,8 | 4,0 | 20,0 | 1,3 | 203,0 | 6,7 |
| Pt | 1,9 | n.a. | 3,0 | <1 | 4,3 | 1,0 | 14,0 | 1,2 | 62,0 | 8,6 |
| Cu/Pd | 25664 | n.a. | 15000 | 7682 | n.a. | n.a. | 1575 | n.a. | 148 | 10448 |

Sample numbers: *1* ) M452397R312 99.15–99.45; *2* ) M452397R305 34.3–34.5; *3* ) VJJA-2017-76.1 (outcrop); *4* ) M452397R313 25.5–25.66; *5* ) VJJA-2017-51.1 (outcrop); *6* ) M452397R314 25.6–25.9; *7* ) M452397R314 15.8–16; *8* ) VJJA-2017-48.1 (outcrop); *9* ) KSM-MUV-06 381.5–381.75; *10* ) S5322017R1 173.65–174.05; samples *8–10* from Järvinen et al. 2010, others from this study.

Elements fro $SiO_2$ to Zr analysed with XRF, from La to Co with ICP-MS, Au to Pt with GFAAS; not analyzed (n.a.).

Cumulus names after Irvine (1982), with intercumulus phases listed as suffix and asterix marking the phase as oikocryst.

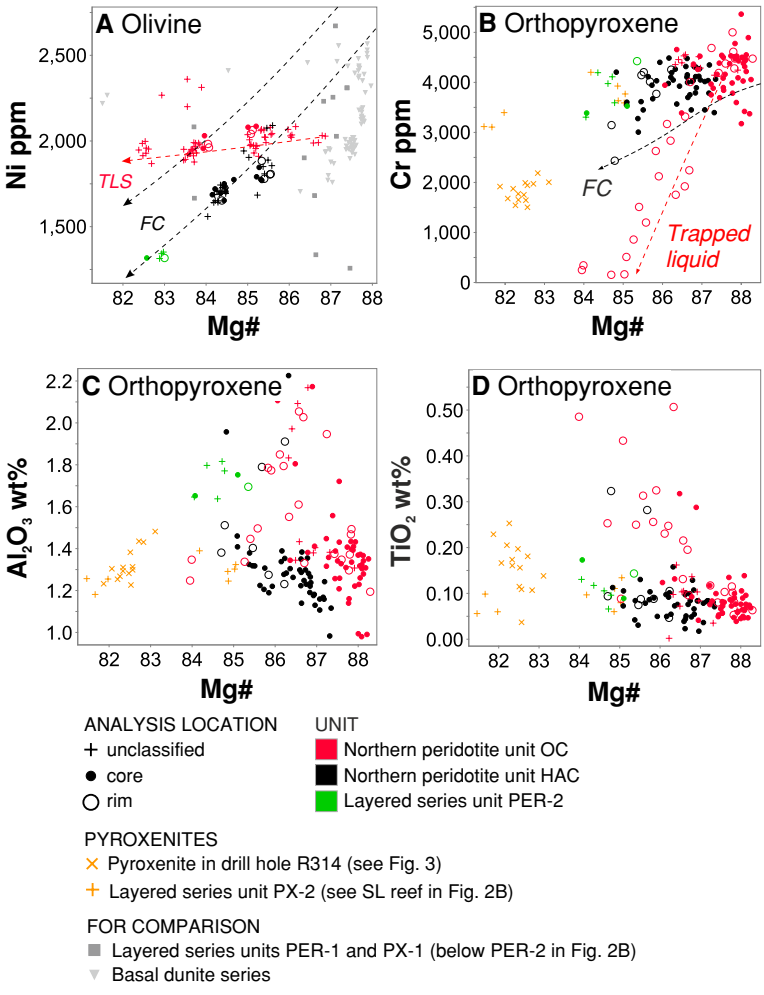


Figure 9. Mineral chemical variation diagrams from the northern peridotites of the Näränkävaara intrusion. **a)** Olivine Mg# vs. Ni. Trend *TLS* illustrates a typical horizontal trapped liquid shift to lower Fo (Barnes 1986a). Trend *FC* is thought to represent combination of trapped liquid shift and fractional crystallization – two black dashed lines show modeled olivine compositions fractionating from a magma of the Näränkävaara marginal series composition, listed in Table 1 (upper line modeled with the Magma Chamber Simulator [Bohrson et al. 2020] using MELTS engine [ver. 1.2.0.; P=0.5 kbar; $FeO/FeO_{tot}$ = 0.9; Gualda et al. 2012]; lower line modeled with COMAGMAT 5.5.2 [Ariskin et al. 2018; P=1 bar; QFM]). **b)** Orthopyroxene Mg# vs. Cr. Trend labeled *Trapped liquid* illustrates the significant Cr-depletion found in core-rim analyses of some poikilitic grains in the OC unit, interpreted as fractional crystallization from a finite volume of trapped liquid. Trend *FC* shows modeled composition of liquidus orthopyroxene fractionating from a Bushveld U-type magma with 12.3 wt.% MgO and 1000 ppm Cr (Barnes 1986a). Note coincidence of unit HAC and PER-2 mineral compositions along modeled fractionation trends in both a and b. **c)** and **d)** Note $Al_2O_3$- and $TiO_2$-rich rim-compositions in the OC unit orthopyroxenes, thought to indicate crystallization from relatively small amount of intercumulus melt, compared to the more homogeneous HAC unit. Comparisons to other units from Telenvuo (2017) and Järvinen et al. (2020, 2021).

## *4.3. Mineral chemical variation*

Representative results of new EPMA spot analyses are presented in Table 2, with sample locations marked in Fig. 3 where possible.

Olivines (Fig. 9a) in the OC unit ($Fo_{82–86.7}$ and 1870–2360 ppm Ni) are, on average, slightly more primitive compared to the HAC unit ($Fo_{83.2–85.9}$ and 1560–2300 ppm Ni). In both units, olivine chadacrysts in pyroxene oikocrysts typically show the highest Fo, Ni, and Cr values. Olivine from the two units display distinct trends in Fig. 9a; olivines from the OC unit plot on a horizontal trapped liquid trend with less variation in Ni content (Barnes 1986a), whereas olivines from the HAC unit plots on a steeper fractional crystallization trend with more variation in Ni at a given Mg#. Note that olivine compositions determined from the PER-2 unit (a single thin section) plot closer to the HAC trend.

Orthopyroxenes (Fig. 9b) in the OC unit ($En_{81–85.1}$ and <20–5360 ppm Cr) are on average slightly more primitive compared to those in the HAC unit ($En_{79–84.6}$ with 2430–5090 ppm Cr). EPMA profiles across orthopyroxene grains (i.e., core-rim analyses) show that zoning in the OC unit is much more pronounced, with single grains typically showing changes of 2000–4000 ppm Cr between

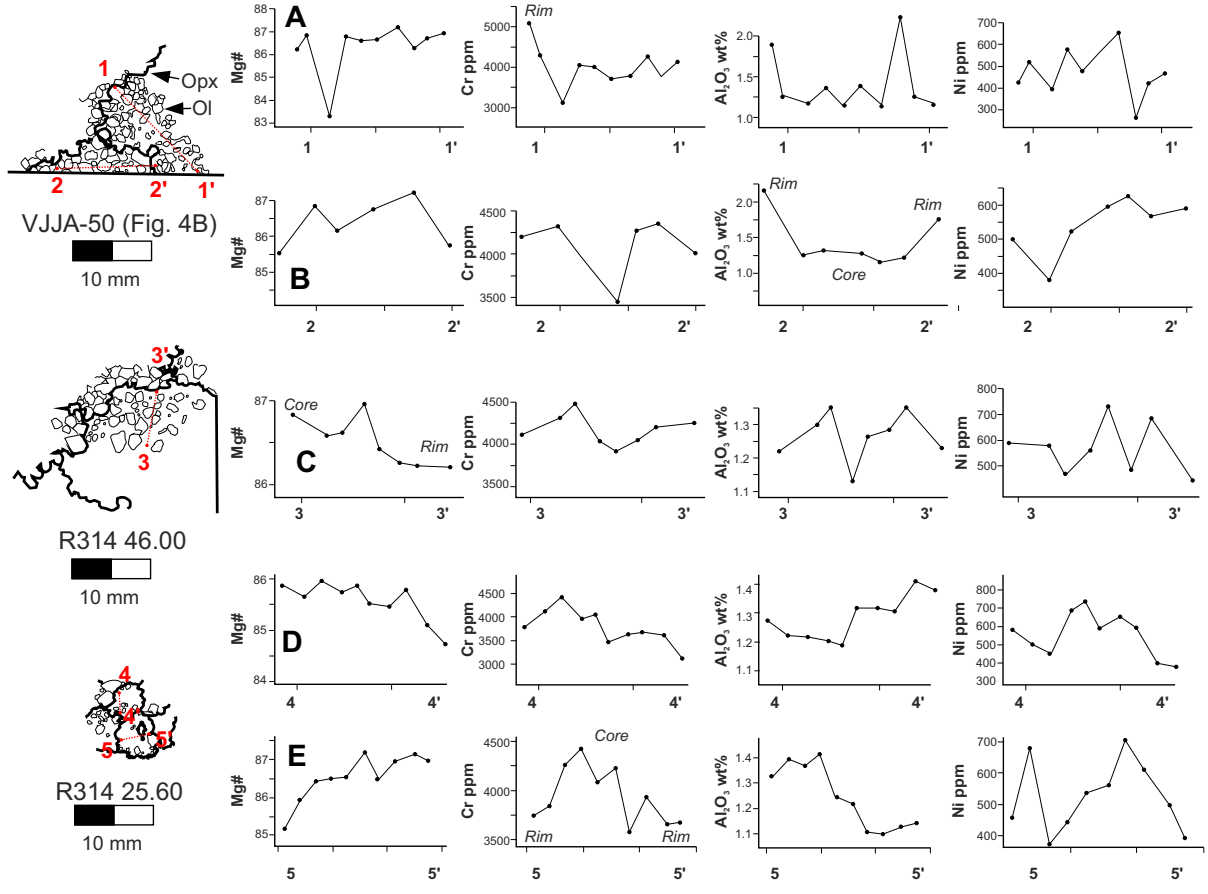


Figure 10. Orthopyroxene core-rim compositions in the HAC unit of the northern peridotites of the Näränkävaara intrusion. Line-drawings show simplified thin-section petrography (thick lines = orthopyroxene; thin lines = olivine); numbered red lines indicate corresponding analysis profiles in **a–e**.

core-rim values (Fig. 9b), with lowest rim-values below detection limit. In contrast, Cr-zoning in the HAC unit is more subdued with core-rim values showing ranges of 500–1500 ppm within single grains. Orthopyroxenes in the OC unit are normally zoned with decreasing Mg# and Cr, and increasing $Al_2O_3$ and $TiO_2$ towards grain rims (Fig. 9b and Table 2). In comparison, orthopyroxenes in the HAC unit show less well-developed and more complex zoning. Typically only Mg# is clearly normally zoned (Fig. 10). In the "oikocrystites", where all analyzed grains are in contact to other orthopyroxene oikocrysts, Cr contents either remains steady or is reversely zoned (Figs. 10a–c), but $Al_2O_3$ and $TiO_2$ are normally zoned ($TiO_2$ not shown). In the granular olivine-pyroxenites adjacent to the pyroxenite contact in R314 (Fig. 4d), orthopyroxenes are normally zoned (Figs. 10d–e). Note that orthopyroxene has only been analyzed from three samples in the HAC unit (Fig. 3), so these trends are poorly constrained.

Clinopyroxenes are diopside and augite with up to 8640 ppm Cr (Table 2); in the OC unit they also show strong normal zoning with Cr, decreasing from core to rim by up to 8000 ppm.

**Table 2:** Results of representative mineral chemical analyses from the Näränkävaara intrusion (pyroxene

| **Series** | | **Northern peridotites** | | | | | | | **Layered series** | | **Northern peridotites** | | **Layered series** | | |
|---|---|---|---|---|---|---|---|---|---|---|---|---|---|---|---|
| **Sample no.** | | *1* | *2* | *3* | *4* | *5* | *6* | *7* | *8* | *9* | *10* | *11* | *12* | *13* | *14* |
| **Unit** | | OC | OC | HAC | HAC | HAC | HAC | R314 pyroxenite | PER-2 | PX-2 | OC | HAC | R314 pyroxenite | PER-2 | PX-2 |
| **Mineral Type** | | Opx Core | Opx Rim | Opx Core | Opx Rim | Opx Core | Opx Rim | Opx Core | Opx Core | Opx Core | Cpx Core | Cpx Core | Cpx Core | Cpx Core | Cpx Core |
| $SiO_2$ | wt. % | 56,55 | 56,00 | 56,36 | 56,57 | 55,66 | 55,63 | 55,66 | 55,79 | 55,30 | 53,96 | 53,43 | 53,01 | 52,95 | 53,38 |
| $TiO_2$ | | <0.067 | 0,247 | <0.067 | <0.067 | 0,090 | 0,101 | <0.067 | 0,173 | 0,109 | 0,174 | 0,272 | 0,300 | 0,146 | 0,198 |
| $Al_2O_3$ | | 1,31 | 1,79 | 1,22 | 1,23 | 1,24 | 1,49 | 1,29 | 1,65 | 1,31 | 2,29 | 2,66 | 2,66 | 2,69 | 2,09 |
| FeO | | 7,79 | 8,84 | 8,54 | 8,94 | 8,79 | 9,43 | 9,50 | 10,31 | 11,13 | 5,86 | 6,10 | 5,53 | 5,59 | 6,09 |
| MnO | | 0,20 | 0,20 | 0,21 | 0,19 | 0,23 | 0,23 | 0,21 | 0,24 | 0,25 | 0,17 | 0,15 | 0,15 | 0,16 | 0,17 |
| MgO | | 32,59 | 30,98 | 31,62 | 31,38 | 32,23 | 30,98 | 29,86 | 30,53 | 29,58 | 21,70 | 20,21 | 18,09 | 19,07 | 18,17 |
| CaO | | 1,69 | 1,96 | 1,79 | 2,07 | 1,16 | 2,00 | 2,73 | 1,38 | 1,85 | 15,23 | 16,44 | 19,40 | 17,94 | 18,63 |
| $Na_2O$ | | <0.05 | 0,05 | <0.05 | <0.05 | 0,06 | 0,05 | 0,07 | 0,08 | *n.a.* | 0,28 | 0,30 | 0,27 | 0,34 | 0,25 |
| Total | | 101,21 | 100,75 | 100,71 | 101,21 | 100,36 | 100,68 | 100,16 | 101,01 | 99,94 | 101,17 | 101,00 | 100,74 | 100,42 | 99,54 |
| Cr | ppm | 4864 | 2817 | 4115 | 4254 | 3724 | 3765 | 3903 | 3366 | 1930 | 7415 | 6927 | 5849 | 7552 | 3074 |
| Sr | | <1175 | <1175 | <1175 | <1175 | 1665 | <1175 | <1175 | 1549 | <1175 | *n.a.* | *n.a.* | *n.a.* | *n.a.* | *n.a.* |
| Ni | | 620 | 479 | 591 | 446 | 566 | 439 | 563 | 512 | 562 | 402 | 382 | 324 | 261 | 259 |
| Co | | <228 | <228 | <228 | 326 | 264 | <228 | <228 | 235 | n.a. | *n.a.* | *n.a.* | *n.a.* | *n.a.* | *n.a.* |
| Mg# | mol. % | 88,2 | 86,2 | 86,8 | 86,2 | 86,7 | 85,4 | 84,9 | 84,1 | 82,6 | 86,9 | 85,5 | 85,4 | 85,9 | 84,2 |
| En | | 85,1 | 82,7 | 83,6 | 82,6 | 84,6 | 81,9 | 80,1 | 81,6 | 79,3 | 60,2 | 56,9 | 51,4 | 54,2 | 51,8 |
| Fs | | 11,7 | 13,5 | 13,0 | 13,5 | 13,2 | 14,3 | 14,6 | 15,8 | 17,1 | 9,4 | 9,9 | 9,0 | 9,1 | 10,0 |
| Wo | | 3,2 | 3,8 | 3,4 | 3,9 | 2,2 | 3,8 | 5,3 | 2,6 | 3,6 | 30,4 | 33,2 | 39,6 | 36,6 | 38,2 |
| Ac | | 0,1 | 0,2 | 0,2 | 0,1 | 0,2 | 0,2 | 0,2 | 0,3 | 0,0 | 1,0 | 1,1 | 1,0 | 1,2 | 0,9 |

Orthopyroxene (Opx); Clinopyroxene (Cpx); Not analyzed (n.a.); See Figs. 2 and 3 for abbreviated unit names.

Sample numbers (spot no.):*1* ) VJJA-76 (1442.2); *2* ) VJJA-76 (1437.2); *3* ) R314 46.0 m (1371.2); *4* ) R314 46.0 m (1380.2); *5* ) R314 25.6 m (1325.2); *6* ) R314 25.6 m (1317.2); *7* ) R314 17.0 m (1257.2); *8* ) VJJA-48 (1476.2); *9* ) MUV-22 12.87 m; *10* ) VJJA-76 (1462.2); *11* ) R314 46.0 m (1368.2); *12* ) R314 17.0 m (1252.2); *13* ) VJJA-48 (1471.2); *14* ) MUV-19 7.85 m; *9* and *14* from Järvinen et al. 2020.

En, Fs, Wo, and Ac are mol. % of cations per formula unit (p.f.u.) normalized to 4 oxygens, e.g., En = $Mg/(Mg+\sout{Fe}+Fe^{3+}+Mn+Ca)$; See S1 for results listed in cations p.f.u.

**Table 2:** (olivines)

| Series | | Northern peridotites | | Layered series |
|---|---|---|---|---|
| **Sample no.** | | *1* | *2* | *3* |
| **Unit** | | OC | HAC | PER-2 |
| **Mineral** | | Olivine | Olivine | Olivine |
| $SiO_2$ | wt. % | 40,99 | 40,62 | 39,57 |
| FeO | | 12,79 | 13,35 | 15,99 |
| MnO | | 0,15 | 0,20 | 0,23 |
| MgO | | 47,16 | 46,42 | 43,80 |
| Total | | 101,61 | 101,18 | 99,82 |
| Cr | ppm | 292 | <154 | <154 |
| Ni | | 2031 | 2306 | 1317 |
| Co | | 386 | 429 | 231 |
| Fo | | 86,7 | 85,9 | 82,8 |

Sample numbers: *1)* R312 8.0 m; *2)* R314 25.60 m; *3)* VJJA-48

**Table 2:** (chromites)

| Series | | Northern peridotites | | | | | Layered series |
|---|---|---|---|---|---|---|---|
| **Sample no.** | | *1* | *2* | *3* | *4* | *5* | *6* |
| **Unit** | | OC | OC | HAC | HAC | R314 pyroxenite | PER-2 |
| **Mineral** | | Chromite | Chromite | Chromite | Chromite | Chromite | Chromite |
| $TiO_2$ | wt. % | 1,79 | 0,76 | 0,84 | 0,23 | 0,34 | 1,75 |
| $Al_2O_3$ | | 5,89 | 12,90 | 7,05 | 16,85 | 4,30 | 1,30 |
| $Cr_2O_3$ | | 31,94 | 33,32 | 33,74 | 35,04 | 47,68 | 28,50 |
| $V_2O_3$ | | 1,24 | 0,75 | 0,31 | 0,18 | 0,69 | 0,26 |
| FeO | | 52,51 | 44,44 | 51,36 | 39,00 | 40,89 | 60,19 |
| MnO | | 0,51 | 0,36 | 0,53 | 0,38 | 0,64 | 0,54 |
| MgO | | 1,89 | 4,28 | 2,16 | 5,54 | 1,66 | 1,08 |
| Total | | 96,22 | 97,41 | 96,52 | 97,67 | 96,72 | 94,28 |
| Ni | ppm | 944 | 1539 | 1149 | 1426 | 345 | 909 |
| Co | | 322 | 326 | 435 | 352 | 490 | 279 |
| Zn | | 2037 | 2654 | 2572 | 1499 | 2546 | 3958 |
| Cr/Σ3+ | mol. % | 40,6 | 40,9 | 42,0 | 42,7 | 64,7 | 35,6 |
| Al/Σ3+ | | 11,2 | 23,6 | 13,1 | 30,6 | 8,7 | 2,4 |
| $Fe^{3+}/\Sigma 3+$ | | 44,7 | 33,8 | 43,6 | 26,2 | 25,4 | 59,6 |
| $Fe^{3+}/Fe_{tot}$ | | 49,3 | 45,9 | 49,3 | 41,4 | 35,9 | 55,5 |
| Mg# | | 9,0 | 19,9 | 10,1 | 25,6 | 8,5 | 5,0 |
| Cr# | | 78,4 | 63,4 | 76,2 | 58,2 | 88,1 | 93,6 |
| $Fe^{3+}$# | | 46,4 | 34,4 | 44,2 | 26,3 | 25,8 | 61,0 |

Sample numbers: *1* ) VJJA-76; *2* ) VJJA-76; *3* ) VJJA-50; *4* ) VJJA-50; *5* ) R314 17.0 m; *6* ) VJJA-48.

$\Sigma 3+ = Cr+Al+Fe^{3+}$; Mg# = $Mg/(Mg+Fe^{2+})$; Cr# = Cr/(Cr+Al);

$Fe^{3+}\# = Fe^{3+}/(Cr+Al+Fe^{3+})$

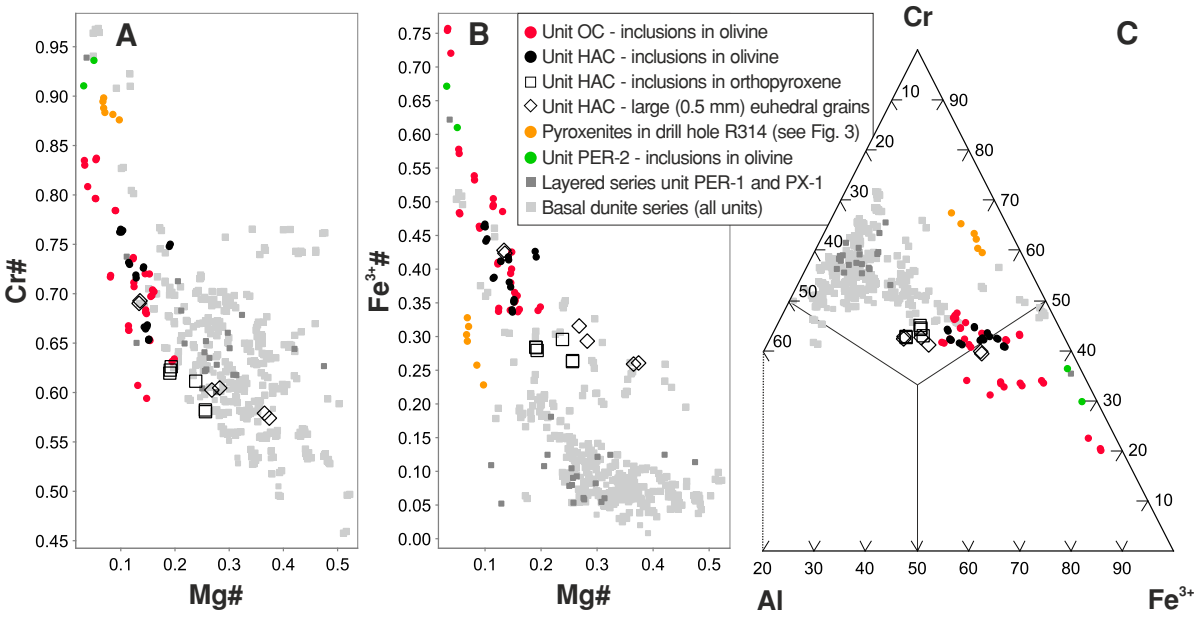


Figure 11. Chromite compositions from the northern peridotites of the Näränkävaara intrusion on **a)** Mg# vs Cr#, **b)** Mg# vs $Fe^{3+}$#, and **c)** Trivalent ion plots. Comparisons to units below PER-2 in stratigraphy from Telenvuo (2017) and Järvinen et al. (2020, 2021).

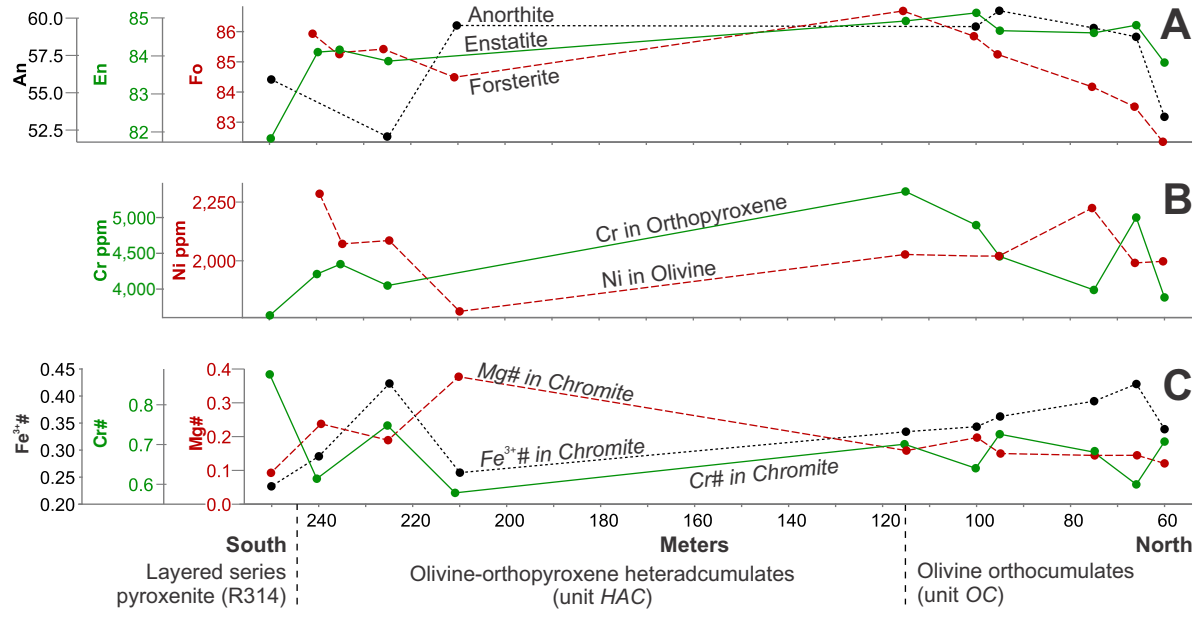


Figure 12. Mineral chemical variations in the northern peridotites over the cross-section in Fig. 3. The most primitive composition analyzed has been plotted for each sample (i.e., highest Mg#, Ni, Cr, An).

Spinels from the OC and HAC units are ferrian chromites, although several analyses with low Mg# and high $Fe^{3+}$# cross over into the magnetite field (Fig. 11). The chromites plot in the field of layered intrusions of Barnes & Roeder (2001) (not shown). The $Fe^{3+}$# values (0.26–0.76) are untypically high for ultramafic rocks. Most analyzed chromites are small ~50 µm inclusions in serpentinized olivines and may have been altered to some degree. However, all chromites show relatively low values of Mn, Co, and Zn with negative correlation against Mg#, thought to be an indication of lack of alteration based on studies of komatiitic cumulates (Barnes 1998). Highest Mg# and lowest $Fe^{3+}$# is found in chromites found either inside orthopyroxenes or as 0.5 mm sized euhedral cumulus grains (Fig. 11).

Mineral chemical trends along the cross section in Fig.3 are presented in Fig. 12. From the northern wall-rock contact southwards, Fo, En, and An contents reach a peak at the border of the OC–HAC units ($Fo_{86.7}$, $En_{85.1}$, $An_{60.5}$), and then generally decrease towards the layered series contact in R314. Chromite $Fe^{3+}$# similarly decreases from the OC unit towards the HAC unit and layered series contact.

# 5. Discussion

The Näränkävaara intrusion comprises the basal dunite series, the layered series, and the previously poorly known northern peridotites (Fig. 2). Because of their great petrographical and geochemical similarities, the northern peridotites were first interpreted as part of the layered series unit PER-2 (Alapieti et al. 1979), and then as part of the orthocumulate margin of the basal dunite series (Alapieti 1982). Here, we aim to constrain the petrogenesis of the northern peridotites based on our new results, and to connect their formation to the emplacement of the magma causing the PER-2 reversal in the layered series.

## *5.1. Initial emplacement and orthocumulate formation as a marginal reversal*

The OC unit shows a well-developed marginal reversal (Latypov 2015) in contact with the Archean basement complex to the north (Fig. 3). With increasing distance from the contact, the marginal reversal is characterized by (1) increasingly adcumulate (or in this case, heteradcumulate) rock types; (2) increasingly primitive (e.g., MgO-richer) whole-rock geochemistry (Fig. 3); and (3) reverse trends in mineral chemistry with, e.g., increasing Fo in olivine away from contact (Fig. 12). Development of similar marginal olivine orthocumulate units up to 200 m thick have previously been described, for example, from the southern contact of the Näränkävaara intrusion (BD-1 in Fig. 2) (Järvinen et al. 2021), as well as from the marginal zones of the 2.44 Ga Burakovsky intrusion (Fig. 1) (Nikolaev & Ariskin 2005) and from the lower contacts of komatiite flows (Gole & Barnes 2020). In intrusions, formation of marginal olivine orthocumulates is commonly attributed to relatively rapid cooling and crystallization against cool wall-rocks, resulting in trapping (and crystallization) of intercumulus melt (Campbell 1987; Latypov 2015). In addition, Latypov (2015) suggested two other processes affecting the generation of marginal reversals in intrusions, namely open-system evolution from increasingly primitive inflowing magmas, and disequilibrium-crystallization in undercooled magma resulting in reverse trends in mineral compositions. The importance of these processes in the OC unit is discussed below.

Whole-rock geochemistry indicates that the OC unit is composed of olivine-melt mixtures (Figs. 5 and 6), with highest proportion of trapped melt nearest to the contact with Archean wall-rocks, where thermal gradients would have been steepest and cooling would have been fastest (Fig. 3c, d). The amount of rapidly crystallized intercumulus material decreases away from the contact, marked by a change from orthocumulus

to heteradcumulus textures in the rocks (Fig. 3b, e). The trend line in the MgO vs. Cr diagram in Fig. 5f does not intersect analyzed olivine compositions but rather passes above them, suggesting that the MgO-rich end-members of the OC unit also contain significant heteradcumulus orthopyroxene, which elevates their whole-rock Cr contents. Both olivine and orthopyroxene have likely been on, or close to, the liquidus when the OC unit magma was emplaced. Nevertheless, the strong normal zoning in the OC unit orthopyroxenes (trend 1 in Fig. 9b) is consistent with pyroxene fractionation from a finite amount of trapped intercumulus melt, indicating that the intercumulus was isolated from the convecting (or flowing) magma relatively early. In a similar manner, olivine chemistry (trend 1 in Fig. 9a) indicates re-equilibration to lower Fo contents during post-cumulus reactions with trapped intercumulus melt (Barnes 1986a). Increasing olivine Fo away from the wall-rock contact (Fig. 12a) correlates with decreasing amount of intercumulus, and is interpreted to primarily reflect the decreasing effect of the trapped liquid shift with distance from the contact (Barnes 1986a). Similar, however more abrupt, mineral chemical trends regarding En and An (Fig. 12) may be related to undercooling and disequilibrium crystallization near the wall-rock contact (Latypov 2015). These observations are interpreted to indicate emplacement and rapid crystallization of the OC unit magma against a cool wall-rock, with geochemical trends primarily related to changes in volume of trapped intercumulus melt.

The composition of the trapped intercumulus melt component in the OC unit can be qualified from whole-rock compositional plots (Chai & Naldrett 1992; Arndt et al. 2008) as an LREE-enriched siliceous high-MgO basalt with approximately 13–15 wt.% MgO (Figs. 5, 6, 8), similar to the melt-representative Näränkävaara marginal series gabbronorite (sample 10 in Table 1). This trapped melt in the OC unit is interpreted as the parental magma composition of the northern peridotites. Note that the relatively high MgO in the ultramafic schists in immediate contact with the basement complex (Fig. 6) indicates a minor proportion of accumulated olivine, crystallized either pre-emplacement or in situ, and therefore this sample is not entirely melt-representative (sample 1 in Table 1).

Lithologically, the OC unit is very similar to the southern olivine orthocumulate margin of the basal dunite series (BD-1 in Fig. 2b). Both orthocumulate units show similar trends in lithology (increasing modal olivine away from basement complex contact) and geochemistry (increasing MgO with decreasing incompatible elements away from basement complex contact; see comparisons in Figs. 5 and 6). Primary differences are that the BD-1 orthocumulate contains slightly more magnesian olivine compared to the OC unit ($Fo_{89–90}$ vs. $Fo_{86–87}$), and that it grades into pure olivine adcumulates instead of olivine-orthopyroxene heteradcumulates (Järvinen et al. 2021). Latypov (2015) argued that parental magma compositions determined from chilled margins and marginal reversals commonly show too low MgO concentrations in relation to the associated intrusion, and that such determinations should be further supported by other methods. In addition to result presented above, parental magma compositions of the Näränkävaara intrusion have been inferred from three other independent sources, as discussed in more detail in Part II of this paper (Järvinen et al. 2022). All results show remarkably similar parental magma compositions (Järvinen et al. 2020, 2021). At least in Näränkävaara, these kind of rapidly cooled olivine orthocumulates can apparently be used to approximate the parental magma compositions quite well (Järvinen et al. 2021, this study). While the basal dunite series shows some evidence for influx of slightly more primitive magma following the initial emplacement of the southern orthocumulate unit (internal evolution from $Fo_{87}$ to $Fo_{90}$;see Järvinen et al. 2021), no such evidence for increasingly primitive magma compositions with progressive influx of magma is found in the northern peridotites (cf. Latypov 2015).

## 5.2. Chromium systematics and oxygen fugacity

As presented here, chromium systematics in the OC and HAC units suggest initial orthopyroxene crystallization from a chromite-saturated magma near the QFM buffer. Ubiquitous small chromite inclusions in olivine indicate that the northern peridotite parental magma was chromite saturated at the time of emplacement. Chromite precipitation buffers the maximum Cr contents in a basaltic magma, primarily as a function of temperature and oxygen fugacity (Murck & Campbell 1986). In addition, the Cr contents of orthopyroxene ($D_{Cr}^{Opx/Liq}$) also varies according to magma Cr contents and oxygen fugacity (Barnes 1986b). The Cr contents in the parental magma of the northern peridotites can be estimated from Fig. 5f to be about 1000 ppm, which is similar to experimental chromite-saturated SHMB melts at QFM (Barnes 1986b; Murck & Campbell 1986). Using the Näränkävaara marginal series gabbronorite as a starting composition (Table 1), fractional crystallization modeling (at P = 0.5–4 kbar and $FeO/FeO_{tot}$ = 0.9) using the Magma Chamber Simulator (MCS; Bohrson et al. 2020) running the MELTS engine (ver 1.2.0.; Gualda et al. 2012) indicates beginning of orthopyroxene crystallization at approximately 1250 °C (full model results in S3). Assuming a QFM oxygen buffer, the partition coefficient for $D_{Cr}^{Opx/Liq}$ at this temperature would be approximately 5 (Barnes 1986b) producing ~5000 ppm Cr in initial orthopyroxene, which is close to that observed in the OC unit (Fig. 9b). Assuming cooling and slight fractionation, the HAC unit orthopyroxenes follow the fractional crystallization model curve of Barnes (1986a) for a typical SHMB magma (trend 2 in Fig. 9b): $D_{Cr}^{Opx/Liq}$ increases with decreasing temperature and compensates for decreasing Cr in the parental melt, resulting in constant Cr contents in pyroxenes with decreasing Mg#.

Chromite $Fe^{3+}$# is sensitive to the oxygen fugacity of the parental magma at the time of chromite crystallization (Murck & Campbell 1986). Chromite $Fe^{3+}$# in the OC and HAC units is high, ranging between 0.25–0.75 (Fig. 11). Even the lowest values correspond to oxygen fugacities above the NNO buffer (Murck & Campbell 1986). Most analyzed chromites in the northern peridotites are ~50 µm sized inclusions in olivines (Fig. 11). Thus they should reflect the composition of a relatively high-temperature magma rather than a late intercumulus melt. However, their compositions may have been significantly modified by post-cumulus re-equilibration processes. Roeder & Campbell (1985) studied similar chromite inclusions in the Jimberlana intrusion, and observed that chromites hosted in olivines in orthocumulate lithologies were highly susceptible to post-cumulus re-equilibration to lower Mg# and higher $Fe^{3+}$#, whereas chromites hosted in either orthopyroxene or in adcumulates were more likely to be closed off from these re-equilibration processes (but could not explain how this happens). Chromites analyzed from the OC unit have likely re-equilibrated to an unknown degree, and we consider their $Fe^{3+}$# values to reflect minimum compositions (Fig. 11). The lowest $Fe^{3+}$# of about 0.25 are found in the HAC unit, in chromites inside orthopyroxenes or as rare relatively coarse euhedral grains (~0.5 mm), and these probably represent near-primary values. Plotting the minimum analyzed $Fe^{3+}$# per sample in Fig. 12c, it can be inferred that oxygen fugacity (proxied by chromite $Fe^{3+}$#) increases towards the contact with the basement complex. We suggest that the initial magmas were close to the QFM oxygen buffer, as presented previously, but the magmas may have become more oxidized closer to the NNO buffer during crystallization of the HAC unit. We suggest that some post-cumulus process, for example oxidizing fluids sourced from wall-rocks, significantly increased the $Fe^{3+}$# in chromites during post-cumulus processes (cf. Roeder & Campbell 1985). Similar high-$Fe^{3+}$# chromites as in the OC unit are also found in the southern orthocumulate margin of the basal dunite series (Fig. 11b). It has been suggested that such rapidly cooled orthocumulate margins have insulated subsequently emplaced magmas from oxidizing wall-rock interactions (Järvinen & Halkoaho 2022).

## 5.3. Heteradcumulate formation

Growing evidence suggests that heteradcumulates are evidence for in situ crystallization, as their poikilitic textures and incompatible-element poor chemical compositions are hard to explain otherwise (Campbell 1987; Godel et al. 2013; Barnes et al. 2016; Latypov et al. 2020). In situ formation of heteradcumulates is summarized after Latypov et al. (2020) as follows. In a fractionating magma, a new phase arriving on the liquidus must become slightly supercooled relative to the magma, because it must overcome the activation energy barrier that is required for the initiation of heterogeneous nucleation. During this supercooling, the magma becomes supersaturated in the chemical components of the new phase, which then results in rapid growth of sparse but coarse poikilitic grains once the new phase nucleates. In layered intrusions, this poikilitic crystal growth is thought to occur at the crystal-melt boundary layer in a manner essentially identical to adcumulus growth, with rejected solute mixed back into the convecting magma. With further cooling of the magma, nucleation rate of the new phase increases, and typical granular cumulus crystallization becomes the controlling mechanism.

The HAC unit is mainly composed of poikilitic Ol-Opx mixtures (Fig. 6) with low concentrations of incompatible elements (Figs. 5g and 8). This indicates that the texturally intercumulus orthopyroxenes have not formed from trapped liquid. In addition, the coarse orthopyroxene oikocrysts show relatively high and constant Cr values in core-rim analyses (Figs. 9 and 10) strongly suggesting that they have formed in continuous contact with a Cr-rich magma.

Most analyzed orthopyroxene oikocrysts in the HAC unit are weakly normally zoned, with decreasing Cr and increasing Al and Ti towards grain rims (Figs. 10c–f). These elements have low rates of diffusion in silicates below liquidus temperatures, thus the zoning patterns most likely indicate fractionation during crystallization. Reverse zoning is also found (Fig. 10a). As these are Cr-rich rims on Opx-Opx contacts they could simply represent closely nucleated grains that grew together early. Alternatively, decreasing temperature and increasing oxygen fugacity significantly increase partitioning of Cr into orthopyroxene (Barnes 1986a), so fluctuations in these variables could be responsible for reverse zoning patterns even in a fractionating magma, with the coupled increase of Cr-Al related to charge balance considerations (Campbell & Borley 1974). Of course, reverse zoning could also be related to magma chamber dynamics, e.g. influx of new magma.

Other mineral chemical trends in the northern peridotites also indicate slight fractionation from the wall-rock contact in the north towards the main body of the intrusion in the south (Fig. 12a, b). On average, the OC unit shows more primitive Fo and En contents compared to the HAC unit (Fig. 9). Fo contents as inferred from whole-rock similarly decrease from the OC to the HAC unit (Fig. 7). The peak-Fo (and En, An) at the border of the OC and HAC units (Fig. 12a) can be interpreted as the cross-over horizon of Latypov (2015), indicating a change from the open-system emplacement of the marginal reversal (unit OC) into a pooled magma chamber undergoing fractional crystallization (unit HAC). However, whole-rock Mg#'s in the HAC unit remain steady suggesting no fractionation of parent magma (Fig. 3a). As will be discussed below, the northern peridotites are linked to the emplacement of the PER-2 unit in the layered series. The PER-2 unit is composed of two olivine-rich peridotitic layers (Fig. 2b), so it is plausible it has been emplaced in several pulses of mafic magma (Järvinen et al. 2020). As speculation, this could explain the generation of a relatively thick harzburgitic heteradcumulate sequence such as the HAC unit with a lack of strong fractionation trends.

Addition of $SiO_2$ is known to expand the stability field of orthopyroxene in a mafic magma and, judging from the orthopyroxene-rich nature of the HAC unit and the extreme "oikocrystites" (Figs. 4b, g), it appears evident that the northern peridotites parental magma has assimilated the felsic

Archean wall-rocks at some stage. Direct evidence for this is the existence of xenoliths and felsic veins in drill core (Fig. 3), which also suggests that at least a part of this contamination has occurred in situ. Minor phlogopite is almost ubiquitous, indicating that the northern peridotites magmas contained $H_2O$, and high chromite $Fe^{3+}$#'s also suggest presence of oxidizing fluids, as previously described. We suggest that the HAC unit formed from a $SiO_2$- and $H_2O$-rich magma. High $H_2O$ concentrations increase diffusion rates of the chemical constituents needed for rapid orthopyroxene growth (Burkhard 2005), and this kind of fluid-fluxed magma could thus also explain the formation of the extreme "oikocrystites" (Fig. 4b). Homogenization of added felsic materials may have occurred before emplacement, based on the general homogeneity of the OC and HAC units. Post-cumulus reactions in ultramafic cumulates, for example magma recharge into crystal-mush and reactive flow, are typically described to produce localized and transgressive percolation zones (Hepworth et al. 2017) or cm-scale percolation channels (Barnes et al. 2016), which are not found. Lastly, the addition of significant external $SiO_2$ into a mafic magma could result in formation of monomineralic chromitites (Irvine 1977). No chromitite-seams have been found, however, which could be related to either relatively small or late addition of felsic materials (below the Opx-Chr peritectic; Barnes 1986b) or that chromitites, if present, are located deeper.

## 5.4. Northern peridotite – pyroxenite contact in R314 and connection to PER-2

The petrogenesis of the northern peridotites has been linked to the basal dunite series (BD-1 in Fig. 2b) (Alapieti 1982) or, alternatively, to the first reversal in the middle of the layered series (PER-2 in Fig. 2b) (Alapieti et al. 1979). Here, connection to the basal dunite is dismissed because of significantly different Fo and Ni contents of olivine in these units (Fig. 9a).

A direct physical connection between the northern peridotites and the PER-2 unit is not observed. The strongest piece of evidence linking them to a common origin is the peridotite–pyroxenite contact in drill hole R314 (Fig. 3), where the HAC unit grades into a fresh plagioclase-websterite (Fig. 4d). A highly similar lithostratigraphic sequence is found in the layered series of the Näränkävaara intrusion, where the PER-2 unit grades into the plagioclase-websteritic unit PX-2 (Fig. 2b). The HAC unit is very similar to the PER-2 unit in terms of both whole-rock (Figs. 5 and 7b) and mineral chemistry (Fig. 9). Same is true for the pyroxenites in drill hole R314 and unit PX-2 and these are also very similar petrographically (Fig. 4e, f). Both pyroxenites are also Pd-enriched (Table 1). The northern peridotites and PER-2 also share similar whole-rock initial $\varepsilon_{Nd}$ (2440 Ma) values of -2 and -2.4 (Järvinen et al. 2022).

A distinct difference between units HAC and PER-2 is that the former contains poikilitic orthopyroxene (Fig. 4b) whereas the latter contains cumulus orthopyroxene (Fig. 4c). As previously discussed, in fractionating magmas a phase commonly appears in poikilitic habit before appearing as an euhedral cumulus phase. From north to south, and following the general model of Latypov et al. (2020), the liquid line of descent of the northern peridotites can be interpreted so that orthopyroxene arrives on the liquidus in the OC unit, remains supercooled (or supersaturated) in the poikilitic HAC unit after initial formation of an insulating orthocumulate margin until nucleation rates increase and "normal" cumulus orthopyroxene crystallization takes over in the R314 pyroxenites. Notably, the HAC and PER-2 units align on same fractionation paths regarding both olivine and orthopyroxene compositions (Fig. 9), suggesting the two are separated by a small amount of fractionation. One possible discrepancy with this hypothesis is that a zone of orthopyroxene overproduction (orthopyroxene adcumulates) would be expected following the beginning of normal granular crystallization (Latypov et al. 2020), whereas only 1–2 meters of olivine-

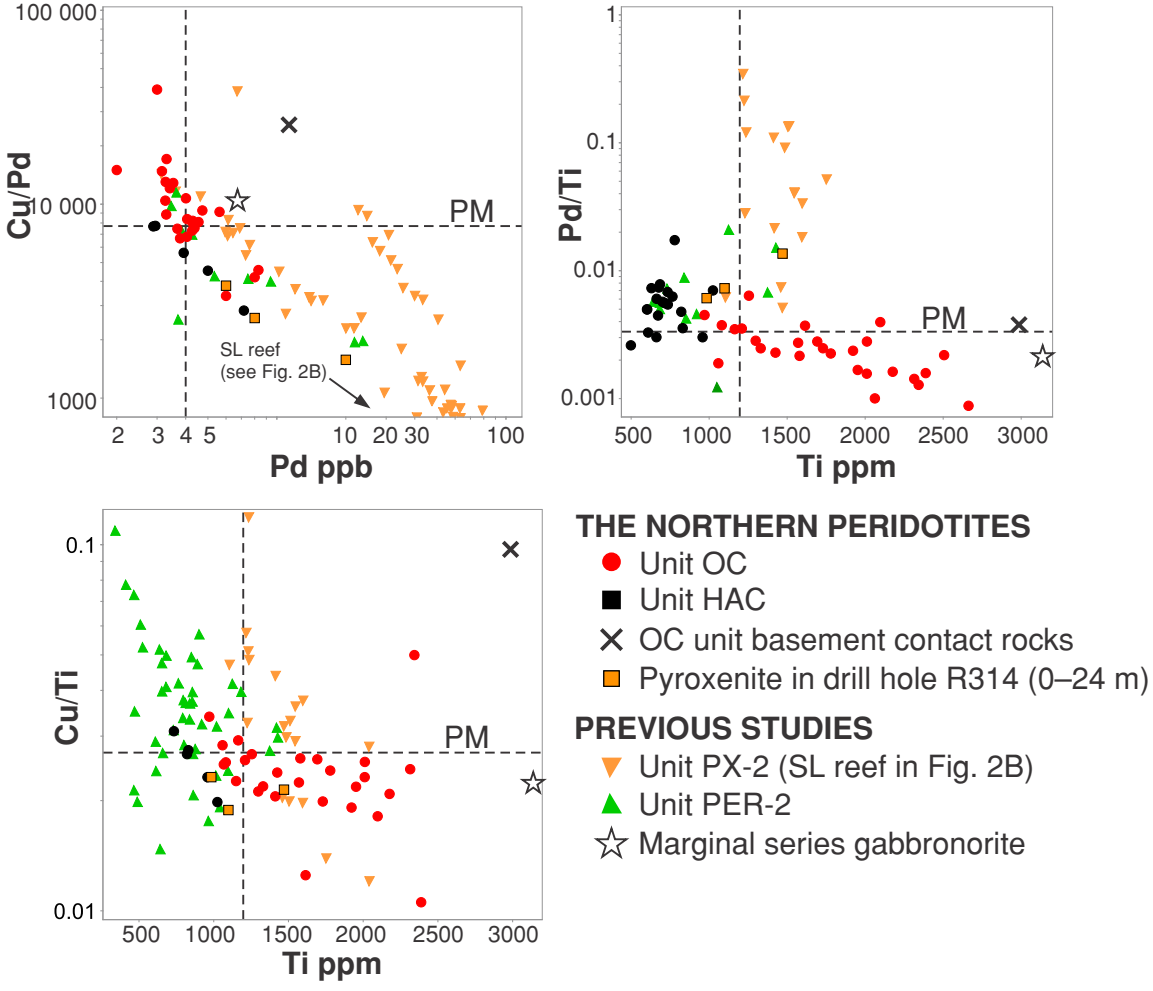


Figure 13. Metal ratios in whole-rocks samples form the northern peridotites of the Näränkävaara intrusion. Dashed lines mark primitive mantle values (McDonough & Sun 1995). Layered series units PER-2 and PX-2 shown for comparison, the latter hosting the sub-economic Salmilammit PGE reef (see Fig. 2b) (Järvinen et al. 2020, 2021).

orthopyroxenites are found at the contact in R314 (Fig. 3).

We conclude that the northern peridotites formed from the same magma causing the PER-2 reversal in the layered series and that the pyroxenites in R314 correlate with the stratigraphic level of the PX-2 unit (Fig. 2b). Their current configuration is related to post-magmatic faulting. The OC unit was formed at the initial emplacement of this magma in the Näränkävaara chamber, and their location is proximal to the PER-2 magma feeder channel likely along the north-side of the intrusion. Because of their position along the northern margin of the intrusion and in contact with the basement complex, the assimilation and cooling history of the northern peridotites was probably somewhat different compared to the PER-2 unit found in the middle of the magma chamber, causing minor lithologic differences. That is, the northern peridotites represent a "marginal facies" of the PER-2 unit.

Alapieti et al. (1979) suggested that the emplacement of the PER-2- magma may have been coincident with a tectonic event creating the large SE-NW fault splitting the intrusion into two blocks. Formation of a relatively fast-cooled orthocumulate margin, like the OC unit, suggests that the basement gneisses must have been relative cool when the northern peridotites (and PER-2) magma was emplaced. A magma chamber of roughly similar size to the present intrusion was most likely in place by the time the northern peridotite (and PER-2) magma was emplaced (Järvinen et al. 2022). Such a chamber would probably have significantly heated the local wall-rocks, and therefore it seems plausible that a significant displacement of wall-rock (allowing for contact with relatively cool wall-rock) was associated with the emplacement of the northern peridotite magma.

Järvinen et al. (2020) suggested that the low grades of the SL reef (Fig. 2b) might be related to emplacement of a PGE-depleted PER-2 magma, diluting the PGE-grades. This hypothesis is disproven by the PER-2 magma composition, which can be inferred from the trapped liquid component in the OC unit to contain metal ratios similar to PM (Fig. 13), indicating no sulfide saturation or PGE depletion has occurred prior to emplacement.

# 6. Conclusions

Our main conclusions are as follows:

- Similar rock types and stratigraphic sequences between the northern peridotites and PER-2 unit strongly suggest that the northern peridotites are linked to the magma causing the first peridotitic reversal in the layered series (unit PER-2).
- The northern peridotite OC unit comprises orthocumulates composed of olivine-melt mixtures and represents the first cumulates formed at the initial emplacement of the PER-2 magma as the magma rapidly cooled against relatively cool Archean wall-rocks.
- The parental magma composition determined for the OC unit is an LREE-enriched siliceous high-Mg basalt very similar to the previous parental magmas inferred for the Näränkävaara layered and basal dunite series. This indicates that the Näränkävaara intrusion has been constructed from multiphase emplacement of high-MgO basaltic magmas.
- Contamination by $SiO_2$-rich melts (partly in situ?) probably resulted in elevated $SiO_2$ and fluid contents, causing rapid growth of cm-scale orthopyroxene oikocrysts in the northern peridotite HAC unit. High Cr concentrations across orthopyroxene oikocrysts suggests they have grown in situ in contact with a Cr-rich magma.
- Similar olivine orthocumulates as the northern peridotite OC unit are found along the southern basement complex contact of the intrusion (in the more primitive basal dunite series). This suggests that magma was initially fed into the Näränkävaara chamber on the southern side of the current intrusion, but that the feeder had moved to the northern side by the emplacement of the PER-2 magma.
- The northern peridotite (or PER-2) parental magmas have undepleted metal ratios suggesting sulfur saturation did not occur prior to emplacement.

# Supplementary data

Electronic Appendices A–C for this article are available via Bulletin of the Geological Society of Finland web page.
Electronic Appendix A: S1 Data package: Analysis results, detection limits, standards used for whole-rock geochemical analyses, and electron microprobe mineral analyses.
Electronic Appendix B: S2 Additional geochemical plots.
Electronic Appendix C: S3 Fractional crystallization modeling results for Näränkävaara parental magma.

## Acknowledgements

The K. H. Renlund Foundation is thanked for providing a working grant to V. Järvinen. We thank the Geological Survey of Finland for providing the materials required for this study, with special thanks to Lassi Pakkanen and Mia Tiljander from the Mineral Chemical Laboratory in Espoo for performing the electron-probe microanalyses. Jarmo Kohonen is thanked for editorial handling of our submission. Rais Latypov and Steve Barnes are thanked for helpful and encouraging reviews.

## Funding sources

V. Järvinen's PhD thesis was funded by the K. H. Renlund Foundation (total of four grants 2017–2020). J.S. Heinonen has benefited from funding by the Academy of Finland (grant 295129).

## References

Akkerman, J. H., 2008. Koillismaa-Naranka project (2005–2007). Geological Survey of Finland, Exploration report, 42 p.

Alapieti, T.,1982. The Koillismaa layered igneous complex, Finland – its structure, mineralogy and geochemistry, with emphasis on the distribution of chromium. Geological Survey of Finland, Bulletin 319, 116 p.

Alapieti, T., Hugg, R., Piirainen, T. & Ruotsalainen A., 1979. The ultramafic and mafic intrusion at Näränkävaara, northeastern Finland. Geological Survey of Finland, Report of Investigation 35, 31 p.

Alapieti, T. & Lahtinen, J., 1986. Stratigraphy, petrology, and platinum-group element mineralization of the early Proterozoic Penikat layered intrusion, northern Finland. Economic Geology 81, 1126–1136. https://doi.org/10.2113/GSECONGEO.81.5.1126

Alapieti, T. T., Kujanpää, J., Lahtinen, J. J. & Papunen, H., 1989. The Kemi Stratiform Chromite Deposit, Northern Finland. Economic Geology 84, 1057–1077. https://doi.org/10.2113/gsecongeo.84.5.1057

Alapieti, T. T., Filén, B. A., Lahtinen, J. J., Lavrov, M. M., Smolkin & V. F., Voitsekhovsky, S. N., 1990. Early Proterozoic Layered Intrusions in the Northeastern Part of the Fennoscandian Shield. Mineralogy and Petrology 42, 1–22. https://doi.org/10.1007/BF01162681

Ariskin, A. A., Bychkov, K. A., Nikolaev, G. S. & Barmina, G. S., 2018. The COMAGMAT-5: Modeling the Effect of Fe-Ni Sulflide Immiscibility in Crystallizing Magmas and Cumulates. Journal of Petrology 59, 283–298. https://doi.org/10.1093/petrology/egy026

Arndt, N., Lesher, C. M. & Barnes, S. J., 2008. Komatiite. Cambridge University Press, Cambridge. 467 p. https://doi.org/10.1017/CBO9780511535550

Barnes, S. J., 1986a. The effect of trapped liquid crystallization on cumulus mineral compositions in layered intrusions. Contributions to Mineralogy and Petrology 93, 524–531. https://doi.org/10.1007/BF00371722

Barnes, S. J., 1986b. The distribution of chromium among opx, spinel (chromite), and silicate liquid at 1 atm. Geochimica et Cosmochimica Acta 50, 1889–1909. https://doi.org/10.1016/0016-7037(86)90246-2

Barnes, S. J., 1998. Chromite in komatiites, 1. Magmatic controls on crystallization and composition. Journal of Petrology 39, 1689–1720. https://doi.org/10.1093/petroj/39.10.1689

Barnes, S. J. & Roeder, P. L., 2001. The of range of spinel compositions in terrestrial mafic and ultramafic rocks. Journal of Petrology 42, 2279–2302. https://doi.org/10.1093/petrology/42.12.2279

Barnes, S. J., Lesher, C. M. & Sproule, R. A., 2007. Geochemistry of komatiites in the Eastern Goldfields Superterrane, Western Australia and the Abitibi greenstone belt, Canada, and implications for the distribution of associated Ni–Cu–PGE deposits. Applied Earth Science 116, 167–187. https://doi.org/10.1179/174327507X271996

Barnes, S. J., David, M. R., Le Vaillant, M., Campbell, M. J., Verrall, M. R, Roberts, M. P. & Evans, N. J., 2016. Poikilitic textures, heteradcumulates and zoned orthopyroxenes in the Ntaka ultramafic complex, Tanzania: Implications for crystallization mechanisms of oikocrysts. Journal of Petrology 57, 1171–1198. https://doi.org/10.1093/petrology/egw036

Bayanova T., Korchagin A., Mitrofanov, A., Serov, P., Ekimova, N., Nitikina, E., Kamensky, I., Elizarov, D. & Huber, M., 2019. Long-Lived Mantle Plume and Polyphase Evolution of Palaeoproterozoic PGE Intrusions in the Fennoscandian Shield. Minerals 9, 22 p. https://doi.org/10.3390/min9010059

Bohrson, W. A., Spera, F. J., Heinonen, J. S., Brown, G. A., Scruggs, M. A., Adams, J. V., Takach, M. K., Zeff, G., Suikkanen, E., 2020. Diagnosing open-system magmatic processes using the Magma Chamber Simulator (MCS): part I—major elements and phase equilibria. Contributions to Mineralogy and Petrology 175, 29 p. https://doi.org/10.1007/s00410-020-01722-z

Burkhard, D. J. M., 2005. Nucleation and growth rates of pyroxene, plagioclase, and Fe-Ti oxides in basalt under atmospheric conditions. European Journal of Mineralogy 17, 675–685.

https://doi.org/10.1127/0935-1221/2005/0017-0675
Campbell, I. H., 1978. Some problems with the cumulus theory. Lithos 11, 311–323. https://doi.org/10.1016/0024-4937(78)90038-5
Campbell, I. H., 1987. Distribution of orthocumulate textures in the Jimberlana intrusion. Journal of Geology 95, 35–53. https://doi.org/10.1086/629105
Campbell, I. H. & Borley, G. D., 1974. The geochemistry of pyroxenes from the Lower Layered Series of the Jimberlana Intrusion, Western Australia. Contributions to Mineralogy and Petrology 47, 281–297. https://doi.org/10.1007/BF00390151
Chai, G. & Naldrett, A. J., 1992. The Jinchuan ultramafic intrusion: Cumulate of a high-Mg basaltic magma. Journal of Petrology 33, 277–303. https://doi.org/10.1093/petrology/33.2.277
Elo, S., 1992. Geophysical indication of deep fractures in the Näränkävaara-Syöte and Kandalaksha-Puolanka zones. In: Silvennoinen, A. (Ed.), Deep fractures in the Paanajärvi-Kuusamo-Kuolajärvi area. Geological Survey of Finland, Special Paper 13, 43–50.
Godel, B., Barnes, S. J. Gürer, D., Austin, P. & Fiorentini, M. L., 2013. Chromite in komatiites: 3D morphologies with implications for crystallization mechanisms. Contributions to Mineralogy and Petrology 165, 173–189. https://doi.org/10.1007/s00410-012-0804-y
Gole, M. J. & Barnes, S. J., 2020. The association between Ni-Cu-PGE sulfide and Ni-Co lateritic ores and volcanic facies within the komatiites of the 2.7 Ga East Yilgarn Craton large igneous province, Western Australia. Ore Geology Reviews 116, 1–21. https://doi.org/10.1016/j.oregeorev.2019.103231
Gualda, G. A. R., Ghiorso, M. S., Lemons, R. V. & Carley T. L., 2012. Rhyolite-MELTS: A modified calibration of MELTS optimized for silica-rich, fluid-bearing magmatic systems. Journal of Petrology 53, 875–890. https://doi.org/10.1093/petrology/egr080
Hepworth, L. N., O'Driscoll, B., Gertisser, R., Daly, J. S. & Emeleus, C. H., 2017. Incremental Construction of the Unit 10 Peridotite, Rum Eastern Layered Intrusion, NW Scotland. Journal of Petrology 58, 137–166. https://doi.org/10.1093/petrology/egx008
Huhtelin, T., 2015. The Kemi chromite deposit. In: Maier W. D. et al. (Eds.), Mineral Deposits of Finland. Elsevier, pp. 165–178. https://doi.org/10.1016/B978-0-12-410438-9.00006-6
Iljina, M., 2003. Hanke 2106001, Pohjois-Suomen kerros-intruusiot 1996–2002, Loppuraportti. Geological Survey of Finland, Report of project, 24 p.
Iljina, M. & Hanski, E., 2005. Layered mafic intrusions of the Tornio-Näränkävaara belt. In: Lehtinen M. et al. (Eds.), Precambrian geology of Finland – key to the evolution of the Fennoscandian Shield. Developments in Precambrian Geology 14. Elsevier, pp. 101–137. https://doi.org/10.1016/S0166-2635(05)80004-0
Iljina, M., Maier, W. D. & Karinen, T., 2015. PGE-(Cu-Ni) Deposits of the Tornio-Näränkävaara Belt of Intrusions (Portimo, Penikat, and Koillismaa). In: Maier, W. D. et al. (Eds.), Mineral Deposits of Finland. Elsevier, pp. 134–164. https://doi.org/10.1016/B978-0-12-410438-9.00005-4
Irvine, T. N., 1977. Origin of chromitite layers in the Muskox intrusion and other stratiform intrusions: A new interpretation. Geology 5, 273–277. https://doi.org/10.1130/0091-7613(1977)5<273:OOCLIT>2.0.CO;2
Irvine, T. N., 1982. Terminology for Layered Intrusions. Journal of Petrology 23, 127–162. https://doi.org/10.1093/petrology/23.2.127-a
Järvinen, V., Halkoaho, T., Konnunaho, J., Heinonen, J. S. & Rämö, O. T., 2020. Parental magma, magmatic stratigraphy, and reef-type PGE enrichment of the 2.44 Ga mafic-ultramafic Näränkävaara layered intrusion, northern Finland. Mineralium Deposita 55, 1535–1560. https://doi.org/10.1007/s00126-019-00934-z
Järvinen, V., Halkoaho, T., Konnunaho, J., Heinonen, J. S. & Rämö, O. T., 2021. The basal dunite of the Precambrian mafic-ultramafic Näränkävaara intrusion: Petrogenetic considerations and implications to exploration. Mineralogy and Petrology 115, 37–61. https://doi.org/10.1007/s00710-020-00725-9
Järvinen, V. & Halkoaho, T., 2022. Formation of poikilitic chromite in the basal dunite series of the 2.44 Ga Näränkävaara layered intrusion. In: Groshev N. Yu. & Yang S. H. (eds.), The Fennoscandian School of Ore Genesis in Layered Intrusions, December 20th, 2021, Online Workshop 2, Extended abstracts, Oulu 2022, pp. 14–17. https://doi.org/10.31241/ARLIN.2021.000
Järvinen, V., Halkoaho, T., Konnunaho, J., Heinonen, J. S., Kamo, S., Davey, S., Bleeker, W., Karinen, T., Rämö, O. T., 2022. Petrogenesis of the Paleoproterozoic Näränkävaara layered intrusion, northern Finland, Part II: U-Pb age and Sm-Nd isotope systematics. Part II submitted simultaneously with the current manuscript to the SGS Bulletin.
Karinen, T., 2010. The Koillismaa Intrusion, northeastern Finland - evidence for PGE reef forming processes in the layered series. Geological Survey of Finland, Bulletin 404, 176 p.
Karinen, T., Hanski, E. & Taipale, A., 2015. The Mustavaara Fe-Ti-V Oxide Deposit. In: Maier, W. D. et al. (Eds.), Mineral Deposits of Finland. Elsevier, Amsterdam, pp. 179–194. https://doi.org/10.1016/B978-0-12-410438-9.00007-8
Karinen, T., Heinonen, S., Konnunaho, J., Salmirinne, H., Lahti, I. & Salo, A., 2021. Koillismaa Deep Hole – Solving the mystery of a geophysical anomaly. In: Kukkonen, I. et al. (eds.), Lithosphere 2021, eleventh symposium on structure, composition and evolution of the lithosphere, Programme and Extended Abstracts, pp. 55–58.

Kulikov, V. S., Bychkova, Y. V., Kulikova, V. V. & Ernst, R., 2010. The Vetreny Poyas (Windy Belt) subprovince of southeastern Fennoscandia: An essential component of the ca. 2.5–2.4 Ga Sumian large igneous provinces. Precambrian Research 183, 589–601. https://doi.org/10.1016/j.precamres.2010.07.011

Lahtinen, J., 2005. Tutkimustyöselostus Näränkävaaran-Murtovaaran ultramafisella-mafisella kompleksilla valtauksilla Murtovaara 6, 8–19, 21–26, 32–34 vuosina 2001–2003 suoritetuista malmitutkimuksista. Geological Survey of Finland, Exploration report, 9 p.

Latypov, R., 2015. Basal Reversals in Mafic Sills and Layered Intrusions. In: Charlier B. et al. (Eds.), Layered Intrusions. Springer, pp. 259–293. https://doi.org/10.1007/978-94-017-9652-1_6

Latypov, R. M., Chistyakova, S. Yu., Namur, O. & Barnes, S. J., 2020. Dynamics of evolving magma chambers: textural and chemical evolution of cumulates at the arrival of new liquidus phases. Earth-Science Reviews 210, 32 p. https://doi.org/10.1016/j.earscirev.2020.103388

Maier, W. D., Halkoaho, T., Huhma, H., Hanski, E. & Barnes, S.-J., 2018. The Penikat Intrusion, Finland: Geochemistry, geochronology, and origin of platinum–palladium reefs. Journal of Petrology 59, 967–1006. https://doi.org/10.1093/petrology/egy051

Makkonen, H. V., Halkoaho, T., Konnunaho, J., Rasilainen, K., Kontinen, A. & Eilu, P., 2017. Ni-(Cu-PGE) deposits in Finland – geology and exploration potential. Ore Geology Reviews 90, 667–696. https://doi.org/10.1016/j.oregeorev.2017.06.008

McDonough, W. F. & Sun, S.-s., 1995. The composition of the Earth. Chemical Geology 120, 223–253. https://doi.org/10.1016/0009-2541(94)00140-4

Murck, B. W. & Campbell, I. H., 1986. The effects of temperature, oxygen fugacity and melt composition on the behaviour of chromium in basic and ultrabasic melts. Geochimica et Cosmochimica Acta 50, 1871–1887. https://doi.org/10.1016/0016-7037(86)90245-0

Nakamura, N., 1974. Determination of REE, Ba, Fe, Mg, Na and K in carbonaceous and ordinary chondrites. Geochimica et Cosmochimica Acta 38, 757–775. https://doi.org/10.1016/0016-7037(74)90149-5

Nikolaev, G. S. & Ariskin, A. A., 2005. Burakovo–Aganozero layered massif in the Trans-Onega area: II. Structure of the marginal series and the estimation of the parental magma composition by geochemical thermometry techniques. Geochemistry International 43, 646–665.

Pearce, T. H., 1968. A contribution to the theory of variation diagrams. Contributions to Mineralogy and Petrology 19, 142–157. https://doi.org/10.1007/BF00635485

Rasilainen, K., Lahtinen, R. & Bornhorst, T. J., 2007. The Rock Geochemical Database of Finland Manual. Geological Survey of Finland, Report of Investigation 164, 38 p.

Roeder, P. L. & Emslie, R. F., 1970. Olivine-liquid equilibrium. Contributions to Mineralogy and Petrology 29, 275–289. https://doi.org/10.1007/BF00371276

Roeder, P. L. & Campbell, I. H., 1985. The Effect of Postcumulus Reactions on Composition of Chrome-spinels from the Jimberlana Intrusion. Journal of Petrology 26, 763–786. https://doi.org/10.1093/petrology/26.3.763

Telenvuo, B., 2017. Kumulusstratigrafia ja mineraalien kryptinen vaihtelu Kuusamon Näränkävaaran kerrosintruusion luoteisosassa. MSc thesis, University of Oulu, 83 p.

Vesanto, J., 2003. Kaivoslain 19 §:n mukainen tutkimustyöelostus Kuusamon Näränkävaaran kerrosintruusion alueella valtauksilla Murtovaara 1–5, 7, 20, 30, 31, 36, 37, 41–71 suoritetuista malmitutkimuksista. Geological Survey of Finland, Exploration report, 9 p.

Wager, L. R., Brown, G. M. & Wadsworth, W. J., 1960. Types of igneous cumulates. Journal of Petrology 1, 73–85. https://doi.org/10.1093/petrology/1.1.73

Whitney, D. L. & Evans, B. W., 2010. Abbreviations for Names of Rock-Forming Minerals. American Mineralogist 95, 185–187. https://doi.org/10.2138/am.2010.3371

Wilson, A. H., 1996. The Great Dyke of Zimbabwe. In: Cawthorn, R. G. (Ed.), Layered Intrusions. Developments in Petrology 15. Elsevier, pp. 365–402. https://doi.org/10.1016/S0167-2894(96)80013-3